Dominant negative and directional dysregulation of Polycomb function in *EZH2*-mutant human growth disorders

Orla Deevy[1], Craig Monger[1], Francesca Matrà[1], Ellen Tuck[1], Eric Conway[2,3], Simona Rodighiero[2], Qi Zhang[4], Chen Davidovich[4,5], Diego Pasini[2,6], Adrian P. Bracken[1,✉]

[1]Smurfit Institute of Genetics, Trinity College Dublin, Ireland
[2]IEO, European Institute of Oncology IRCCS, Department of Experimental Oncology, Via Adamello 16, 20139 Milan, Italy
[3]School of Biomolecular and Biomedical Science, University College Dublin, Dublin 4, Ireland
[4]Department of Biochemistry and Molecular Biology, Biomedicine Discovery Institute, Faculty of Medicine, Nursing and Health Sciences, Monash University, Clayton, VIC, Australia
[5]EMBL-Australia and the ARC Centre of Excellence in Advanced Molecular Imaging, Clayton, VIC, Australia
[6]University of Milan, Via A. di Rudini 8, Department of Health Sciences, 20142 Milan, Italy
✉Corresponding author: adrian.bracken@tcd.ie

Weaver syndrome (WS) is a developmental overgrowth and intellectual disability disorder caused by heterozygous mutations in EZH2. EZH2 encodes the enzymatic subunit of Polycomb Repressive Complex 2 (PRC2) which mediates methylation of histone H3 lysine residue 27 (H3K27). Although PRC2 has been extensively studied at the molecular level, the effects of WS-associated EZH2 mutations on cells remain poorly understood. In this study, we expressed WS-associated EZH2 variants in mouse embryonic stem cells and found that they have dominant negative effects on Polycomb repressive function. These EZH2 variants decrease H3K27me2/3 and increase H3K27ac levels at intergenic regions, causing global chromatin decompaction and transcriptional upregulation of sensitive Polycomb target genes. Interestingly, a contrasting EZH2 variant linked to growth restriction caused opposing changes in H3K27 methylation and acetylation, and repressed the same cohort of Polycomb target genes. Our study provides insights into the molecular mechanisms of EZH2-mutant human growth disorders, revealing the opposing changes in chromatin and transcription associated with Weaver syndrome and growth restriction, respectively.

Introduction

Polycomb Repressive Complex 2 (PRC2) is a highly conserved chromatin regulatory complex essential for lineage specification and cellular memory in multicellular organisms[1–3]. Mammalian PRC2 consists of three core subunits – SUZ12, EED, and either the EZH1 or EZH2 histone methyltransferase (HMTs) – which together catalyse the deposition of up to three methyl groups on histone H3 at lysine 27 (H3K27). This trimeric core of PRC2 interacts with accessory proteins that facilitate its recruitment to chromatin and modulate its methyltransferase activity[3,4]. Both core and accessory PRC2 components are essential for normal mammalian development[5]. PRC2 broadly deposits H3K27me3 across transcriptionally silent developmental gene promoters[6–8]. The H3K27me3 modification is believed to promote the recruitment of at least some forms of the canonical Polycomb Repressive Complex 1 (cPRC1) via specific interaction with its constituent CBX proteins[9,10]. The recruited cPRC1 then promotes chromatin compaction and transcriptional repression[9]. The functions of PRC2-mediated H3K27me1 and H3K27me2 are less well understood. While H3K27me1 is localised along actively transcribed gene bodies[11,12], H3K27me2 is extensively deposited throughout intergenic regions of the genome[13,14]. This broad deposition profile of H3K27me2 prompted us to propose it could function as a repressive "blanket" to counter H3K27ac accumulation and/or to restrict the inappropriate activation of enhancers of alternative lineages[11–13].

Heterozygous mutations in the *EZH2*, *EED* and *SUZ12* genes cause a triad of congenital overgrowth and intellectual disability (OGID) syndromes with highly overlapping clinical presentations – Weaver syndrome (MIM #277590; WS), Cohen-Gibson syndrome (MIM #617561; COGIS), and Imagawa-Matsumoto syndrome (MIM #618786; IMMAS), respectively. These PRC2-related overgrowth syndromes are rare, with collectively less than 100 cases reported to-date[15–17]. However, it is likely that their true incidence is underestimated as a result of their very wide clinical presentation, which most often includes pre- and post-natal overgrowth, tall stature, advanced bone age, variable intellectual disability, and a subtle but characteristic facial appearance[15,18]. Weaver syndrome is the most extensively studied PRC2-related overgrowth syndrome, with *EZH2* first reported as the causative gene in 2011, and approximately sixty individuals reported to date[19,20]. Intriguingly, Weaver syndrome-associated *EZH2* mutations are predominantly missense variants, with the majority affecting its catalytic SET domain, though some fall within its CXC and SANT domains[21]. Rare nonsense mutations have also been reported in Weaver syndrome, which all occur within the last exon of *EZH2* and are therefore likely to escape nonsense-mediated decay at the mRNA level, meaning a truncated EZH2 mutant variant will be expressed[22,23]. The lack of nonsense mutations in more N-terminal exons of *EZH2* suggests haploinsufficiency is unlikely to be the major mutational mechanism of Weaver syndrome. Despite this, Weaver syndrome-associated EZH2

missense variants are predominantly considered loss-of-function hypomorphs due to their reduced activity in *in vitro* histone methyltransferase assays[21,23–25]. In contrast to Weaver syndrome-associated EZH2 missense variants, IMMAS overgrowth can be caused by both missense and premature termination codon mutations in the *SUZ12* gene. These premature termination codon mutations are predicted to result in nonsense-mediated decay and thus no protein expression from the mutant allele, implicating haploinsufficiency as the mutational mechanism in IMMAS[16]. It is not understood why the mutational profile of genes encoding proteins from the same PRC2 complex are different in these clinically similar disorders.

Strikingly, a heterozygous missense mutation of *EZH2* (p.A738T) is implicated in an opposing developmental phenotype characterized by growth restriction[26]. This EZH2 variant has increased histone methyltransferase activity *in vitro* and is therefore considered to be a gain-of-function (GoF) variant. Functional studies of EZH2 variants associated with Weaver syndrome or growth restriction have mainly employed *in vitro* histone methyltransferase assays, DNA methylation profiling, or assays of global H3K27 methylation[23–26]. However, these *in vitro* assays and global assessments of H3K27 methylation levels do not capture the complexity of the Polycomb system. In particular, they lack analyses of the genome-wide profiles of all three H3K27 methylation states in cells, including on Polycomb target genes, and do not consider the possible consequences on cPRC1 recruitment and target gene expression. As has been demonstrated for several cancer types in which PRC2 function is disrupted, the precise mapping of H3K27 methylations, coupled with gene expression changes, is critical to understanding disease aetiology[13,27–29]. Furthermore, we previously proposed that the potential disruption of intergenic H3K27me2/3 could contribute to the aetiology of Weaver syndrome[5], and we now speculate it may also be central to the aetiology of *EZH2*-associated growth restriction.

Here we explore the consequences of *EZH2* mutations associated with opposing Weaver and growth restriction syndromes on the genome-wide functions of PRC2 in mouse embryonic stem cells (ESCs). We show that Weaver syndrome-associated EZH2 variants act in a dominant negative manner. Furthermore, we identify directly opposing disruptions to PRC2 function, and directly opposing transcriptional changes caused by EZH2 mutations associated with Weaver syndrome versus *EZH2*-associated growth restriction, which we propose are central to their opposing aetiologies. Taken together, our results further highlight how the precise equilibrium in H3K27 methylations is crucial for the regulation of growth during development.

Results

Weaver syndrome-associated EZH2 variants cause dominant negative global reductions in H3K27me3

We sought to perform a functional investigation of *EZH2* mutations associated with Weaver syndrome (WS) using mouse embryonic stem cell (ESCs) lines stably expressing individual variants. An extensive literature review identified 67 individuals diagnosed with Weaver syndrome who were reported to have a coding mutation in *EZH2* (Fig. 1a and Table 1). Amongst this group, 64 presented with non-synonymous variants affecting 34 different residues within EZH2, while 3 individuals had mutations resulting in premature stop codons. Supporting impairment of histone methyltransferase activity as a central mechanism, the single amino acid variants tend to cluster around the SET and SRM domains of EZH2, which together interact with the histone H3 tail substrate to mediate H3K27 methylation (Fig. 1b).

We chose ten EZH2 mutations to investigate, which are broadly reflective of the genetic and phenotypic heterogeneity of Weaver Syndrome (Fig. 2b). We generated *Ezh2* heterozygous knockout mouse ESCs (Extended Data Fig. 1a-c), and then exogenously expressed FLAG-tagged EZH2 variants in these cells by lentiviral transduction (Fig. 2a). We also expressed a wild-type EZH2 control and, for comparison, the oncogenic EZH2-Y641F variant. EZH2-Y641F occurs in lymphoma and has a well-characterised gain-of-function effect such that it increases H3K27me3 and reduces H3K27me2 when expressed in cells[13,30,31]. All exogenous EZH2 proteins were expressed at equal levels in this system, and the overall EZH2 protein abundance was comparable to that of endogenous EZH2 in the parental cell line (Fig. 2b-c).

Immunoblot analyses for H3K27 methylation showed that 9/10 of the reported Weaver syndrome-associated EZH2 variants caused globally decreased H3K27me3 (Fig. 2b-c). On closer inspection of the original reporting article, the EZH2-D233V variant (variant 5) with unchanged H3K27me3 was associated with a mild clinical presentation of Weaver syndrome[21], supporting the utility of this cellular assay. Importantly, the H3K27me3 reductions caused by the 9 other Weaver syndrome-associated EZH2 variants occurred in a dominant-negative manner since the average decrease was more severe than in the *Ezh2*$^{fl/\Delta}$ heterozygote knockout cell line (Fig. 2b-c). This was surprising because, when expressed in *Ezh1/2* double knockout ESCs which lack all H3K27 methylation [32], all 9 Weaver syndrome-associated variants possessed some degree of H3K27 methyltransferase activity (Extended Data Fig. 1d-f), supporting partial but not total loss-of-function. However, we did not see any additive effects of the activity of these variants when expressed in the *Ezh2*$^{fl/\Delta}$ heterozygote, and instead observed negative interference on the activity of the

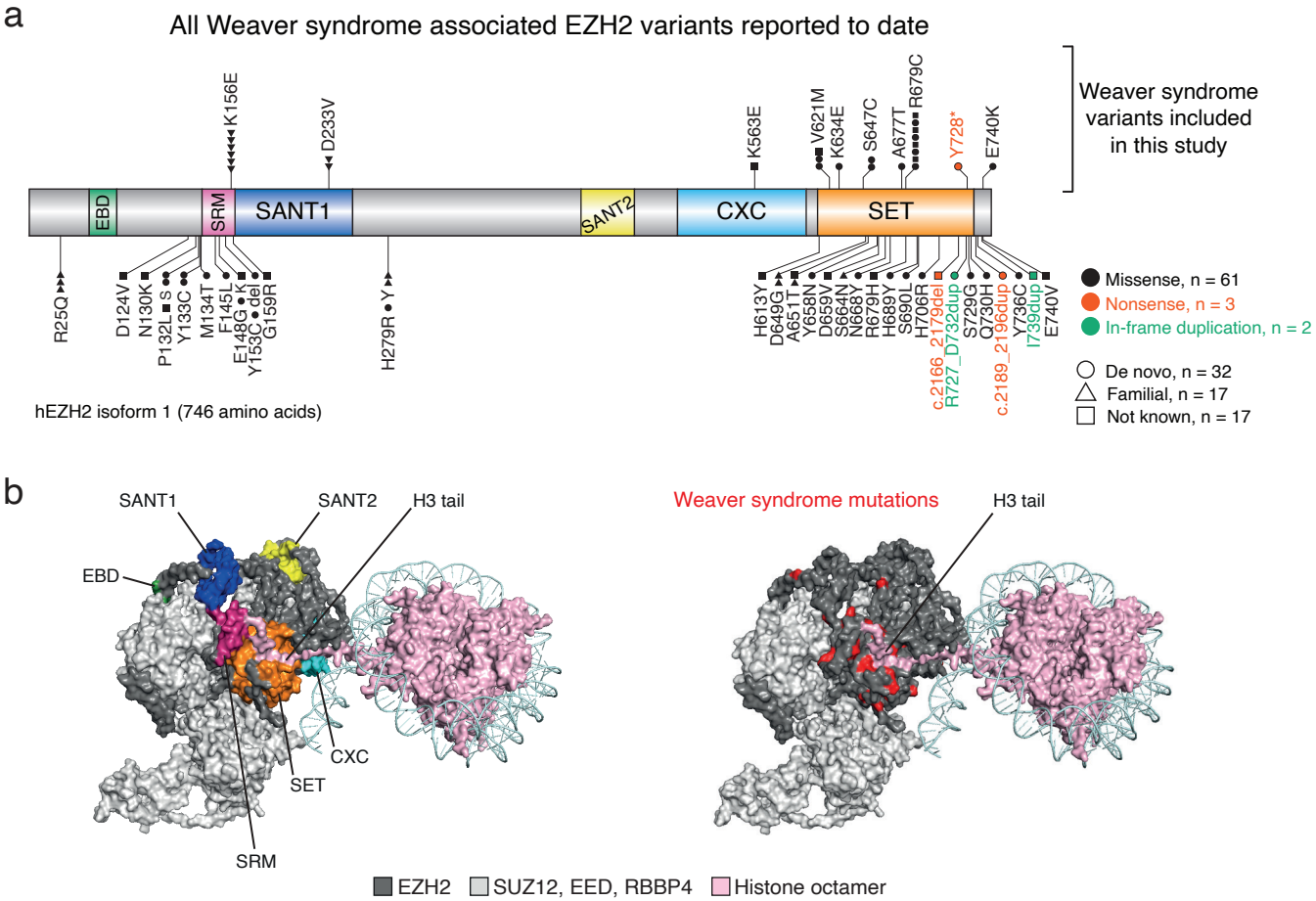

Figure 1. Weaver syndrome-associated EZH2 mutations cluster in domains proximal to the histone H3 tail substrate. a. Schematic of the human EZH2 protein (isoform 1; Q15910-1) summarising the distribution of coding variants reported in Weaver syndrome, highlighting those included in this study (see Table 1 for source citations). Missense variants are indicated in black, nonsense variants in red, and in-frame duplications in green. Each shape represents an affected individual with a pathogenic mutation in EZH2 that is either de novo (circle), familial (triangle), or of unknown inheritance status (square). EBD = EED-binding domain; SRM = stimulatory response motif. **b**. Cryo-EM structure of PRC2.2 bound to a H2AK119ub1-modified nucleosome, with EZH2 shown in dark grey, and EED and SUZ12 in light grey for clarity (PDB: 6WKR, Kasinath et al., 2021). (Left) EZH2 domains are highlighted as per panel (a) above: EBD (light green), SRM (hot pink), SANT1 (dark blue), SANT2 (yellow), CXC (cyan) and SET (orange). (Right) Amino acids affected by Weaver syndrome mutations are highlighted in red. Nucleosome DNA is shown in pale cyan and the histone octamer is shown in light pink.

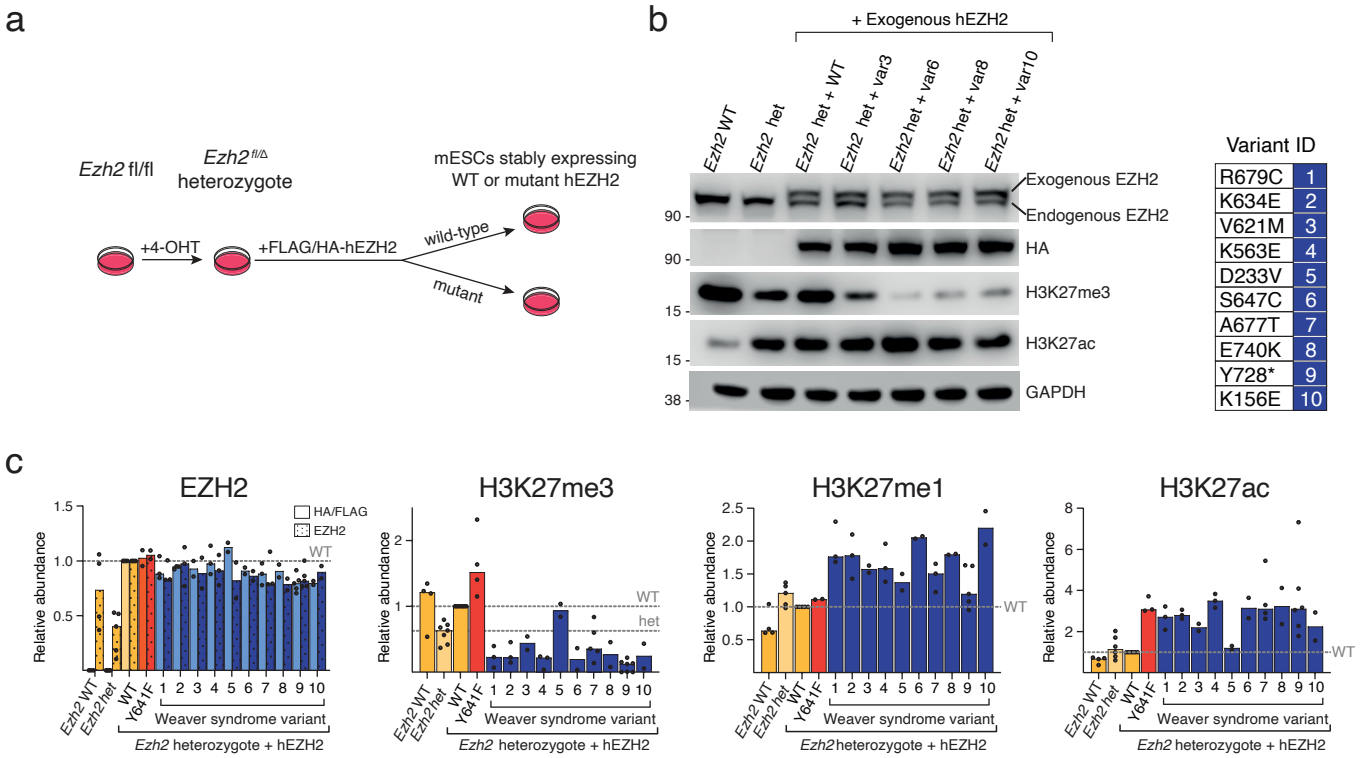

Figure 2. Weaver syndrome-associated EZH2 variants dominant negatively impair global PRC2 activity. a. Schematic of the isogenic stem cell model system used to generate the data presented in panels (b) and (c), and for all subsequent figures. **b.** Representative immunoblots for HA, EZH2 and H3K27 modifications states, probing whole cell lysates from the indicated cell lines. GAPDH is shown as a loading control. **c**. Relative quantification of immunoblot analyses of EZH2 and the HA/FLAG epitope tag, H3K27me3, H3K27me1 and H3K27ac abundance in the indicated cell lines. Signal intensity values were normalized to a loading control and then expressed relative to the Ezh2fl/Δ + hEZH2WT cell line. The dashed lines represent the normalised Ezh2$^{fl/\Delta}$ (het) and Ezh2$^{fl/\Delta}$ + hEZH2-WT (WT) values. Data values represent independent biological replicates whose median values are plotted as bars.

endogenous wild-type allele (Fig. 2b-c). Additionally, the strong global reductions in H3K27me3 observed in the 9 Weaver syndrome-associated EZH2 variants were associated with 2-3 fold increases in global H3K27 acetylation (Fig. 2b-c). The EZH2-D233V variant was again the outlier, which resembled wild-type EZH2 in this assay. Collectively, these data support dominant negative effects on global H3K27me3 levels as a shared mechanism across Weaver syndrome-associated EZH2 variants.

Weaver syndrome-associated EZH2 variants differ in their effects on H3K27me3 at Polycomb target genes

We next sought to examine the consequences of Weaver syndrome-associated *EZH2* mutations on the ability of PRC2 to deposit H3K27me3 at Polycomb target genes (Fig. 3a). We focused on a subset of 5 Weaver syndrome-associated EZH2 variants (Fig. 3b), selected based on their frequency of occurrence, striking clinical phenotype, or both: R679C (variant 1), K634E (variant 2), K563E (variant 4), A677T (variant 7) and Y728* (variant 9). We performed exogenous reference genome-normalised ChIP-seq (ChIP-Rx) of H3K27me3 and H3K27me2, and FLAG (FLAG-EZH2). Four of the EZH2 variants had reduced average levels of H3K27me3 at Polycomb target gene promoters but, surprisingly, the EZH2-A677T variant had moderate average increases in H3K27me3 deposition at these loci (Fig. 3c-d). We observed converse changes in average H3K27me2 levels at Polycomb target promoters, such that 4/5 EZH2 variants had increased levels of H3K27me2, whereas the EZH2-A677T variant had reduced H3K27me2 at these sites (Fig. 3c-d). We noted that the pattern of increased H3K27me3 and reduced H3K27me2 at Polycomb target genes caused by the EZH2-A677T variant was similar to, albeit less profound than, the oncogenic gain-of-function EZH2-Y641F variant that has enhanced ability to convert H3K27me2 to H3K27me3 (Extended Data Fig. 2a-b). Supporting this, structural modelling of *in silico* mutated EZH2 hints at an analogous mutational effect potentially underpinning the similarities between EZH2-A677T and EZH2-Y641F (Extended Data Fig. 2c). Specifically, A677T is expected to cause steric clashes with Y641 (red discs in Extended Data Fig. 2c, centre). This could in turn shift Y641 and therefore enlarge the lysine channel, as predicted to occur when Y641 loses its hydroxyl group in the case of the Y641F variant (Extended Data Fig. 2c, right), and as previously proposed in the case of the lymphoma-associated mutation EZH2-Y677G[30].

Taken together, these data indicate that while most (4/5 tested) Weaver syndrome-associated EZH2 variants reduce the ability of PRC2 to deposit H3K27me3 at Polycomb target genes, this is not true for all. As such, we speculate that the presumed global dysregulation of PRC2-mediated H3K27me3 deposition at Polycomb target genes is not the critical common factor driving the Weaver Syndrome phenotype.

Weaver syndrome-associated EZH2 variants cause reductions in intergenic H3K27 methylations coupled with chromatin decompaction

To test our hypothesis that Weaver syndrome-associated EZH2 mutations lead to defects in H3K27 methylation at intergenic regions[5], we analysed our genome-wide ChIP-Rx data for H3K27me2 and H3K27me3 and focussed on intergenic chromatin regions (Fig. 4a). We additionally performed and analysed a matched ChIP-Rx of H3K27ac, a histone modification enriched at transcriptionally active regions and mutually exclusive from H3K27me2/3[13]. We found that all 5 studied Weaver syndrome-associated EZH2 variants exhibited globally reduced levels of H3K27me2/3, which can be seen along the length of chromosome 9 as an example (Fig. 4Bb and Extended Data Fig. 3a). Next, we specifically examined gene bodies and intergenic regions and found that all five Weaver syndrome-associated EZH2 variants had reduced H3K27me2/3 at both intergenic and gene-body regions (Fig. 4c and Extended Data Fig. 3b). All EZH2 variants exhibited lower intergenic and gene-body H3K27me2 levels compared to the *Ezh2*$^{fl/\Delta}$ heterozygote, highlighting potential dominant-negative effects of the Weaver syndrome-associated EZH2 mutations. Notably, the EZH2-A677T variant was the only one that did not also display lower levels of H3K27me3 at intergenic and gene-body regions compared to the *Ezh2*$^{fl/\Delta}$ heterozygote control. All 5 Weaver syndrome-associated EZH2 mutations caused increased levels of H3K27ac at both intergenic and gene-body regions (Fig. 4b-c and Extended Data Fig. 3a-b), in line with the global increases observed by immunoblot analysis (Fig. 2b-c). Furthermore, H3K27ac had a tendency to increase wherever H3K27me3 or H3K27me2 decreased, suggesting that the reductions in H3K27 methylations increase substrate availability for acetylation (Fig. 4d and Extended Data Fig. 3d).

We next wanted to investigate whether these global reductions in H3K27me2/3, combined with increased H3K27ac, associate with changes in chromatin architecture. To do this, we performed H3 staining followed by stochastic optical reconstruction microscopy (STORM) imaging. This technique has been used previously to measure chromatin architecture through the distribution of nucleosomes into clusters[33]. Weaver syndrome-associated EZH2 variants resulted in chromatin decompaction of nucleosomes from clusters, as observed by the more diffuse histone H3 signal in representative images (Fig. 4e). Together with quantitative measures showing histone H3 being present in fewer and less densely packed clusters, this suggests that chromatin is less densely packed in cells expressing Weaver syndrome-associated EZH2 variants. Taken together, these

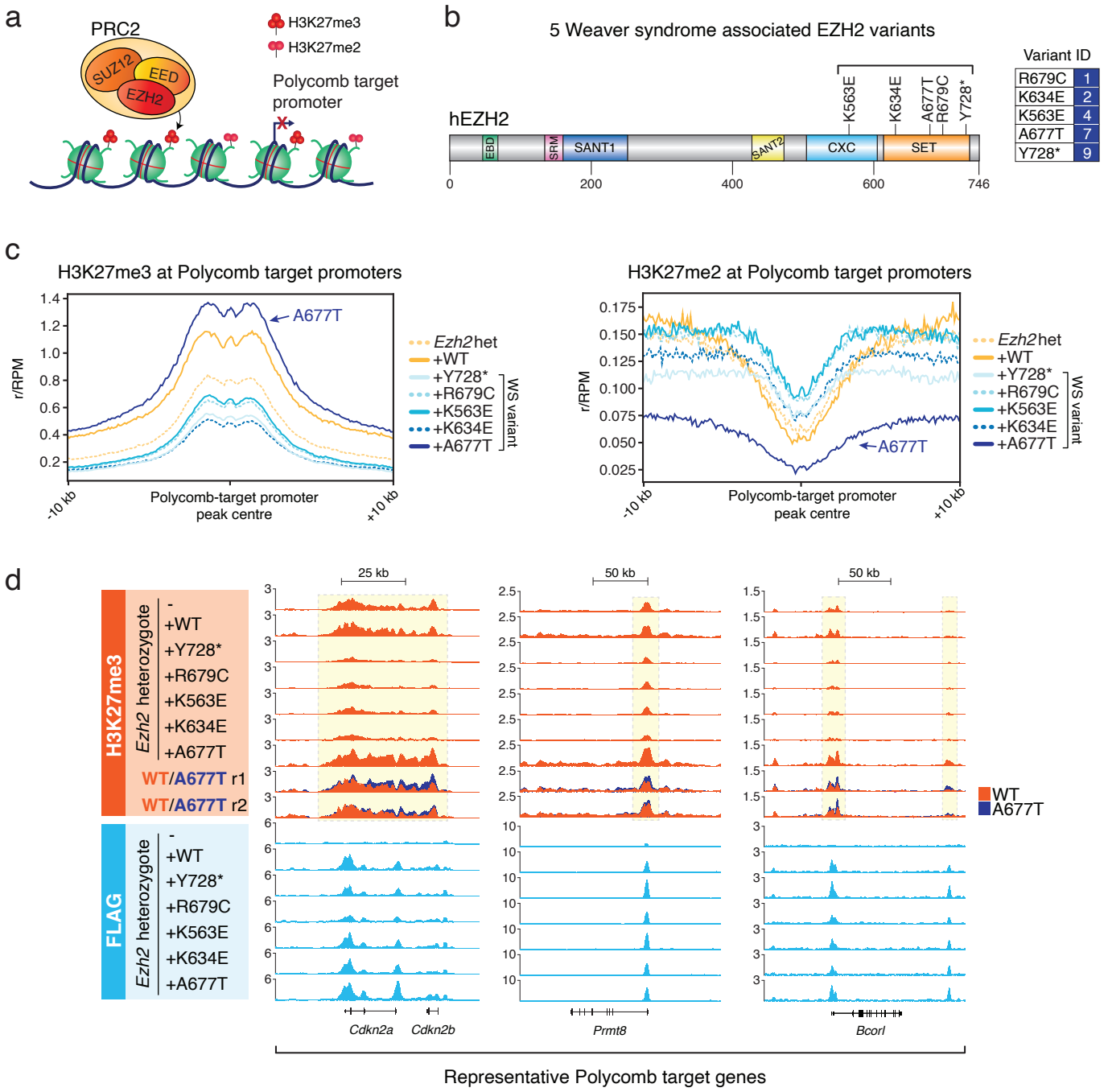

Figure 3. Weaver syndrome-associated EZH2 variants differ in their effects on H3K27me3 at Polycomb target genes. a. Schematic illustrating PRC2-mediated H3K27me3 deposition at Polycomb target genes. **b**. Schematic of the human EZH2 protein (isoform 1; Q15910-1) highlighting the five Weaver syndrome-associated variants selected for further study. **c**. Average ChIP-Rx signal profiles for H3K27me3 (left) and H3K27me2 (right) at Polycomb target promoters (n = 3870) in the indicated cell lines. Control cell lines are coloured in yellows while cells expressing Weaver syndrome EZH2 variants are coloured in blues. **d**. UCSC genome browser tracks showing ChIP-Rx normalised reads of H3K27me3 (top) and FLAG (bottom) at the indicated Polycomb target gene loci (*Prmt8, Bcorl, Cdkn2a/b*) in Ezh2$^{fl/\Delta}$ ESCs with or without stable transgenic expression of indicated FLAG-tagged EZH2 constructs. Also shown are overlayed tracks from two biologically independent ChIP-Rx experiments (r1 = replicate 1, r2 = replicate 2), directly comparing the H3K27me3 enrichment from the cell lines expressing either EZH2-WT (red) or EZH2-A677T (blue).

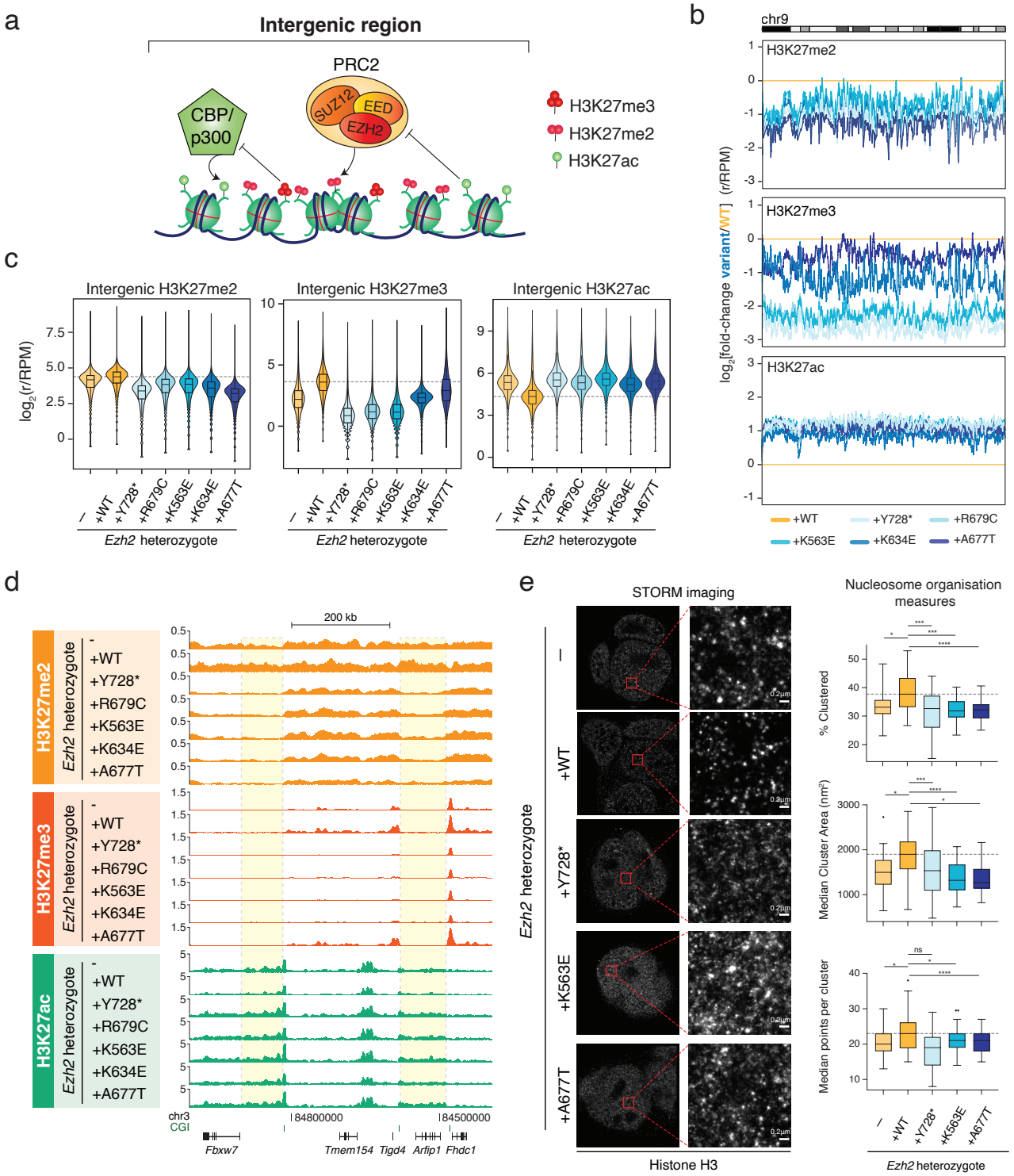

Figure 4. Weaver syndrome-associated EZH2 variants alter the intergenic landscape of H3K27 modifications and chromatin compaction. a. Schematic illustrating the predominant H3K27 methylation states mediated by PRC2 at Polycomb target genes (left; H3K27me3) versus intergenic regions (right; H3K27me2). Also depicted is the antagonistic relationship between PRC2-mediated H3K27me2/3 and CPB/p300-mediated H3K27ac. **b.** Rolling average plots presenting the fold change in H3K27me2, H3K27me3 and H3K27ac ChIP-Rx signal in cells expressing WS EZH2 variants compared to EZH2-WT across the whole of chromosome 9. **c.** Violin plot representations of the log2 ChIP-Rx normalized reads per million (r/RPM) of H3K27me2, H3K27me3, and H3K27ac enrichments in the indicated cell lines across 188,538 10kb bins representing all intergenic regions. The dashed lines represent the EZH2-WT rescue cell line values. **d.** UCSC genome browser tracks showing ChIP-Rx normalised reads of H3K27me2, H3K27me3 and H3K27ac at a ~600 kb genomic locus in the indicated cell lines. This locus includes a repressed PRC2 target gene (*Fhdc1*), two active genes (*Arfip1, Fbxw7*) and intervening non-genic regions. Representative gene body and intergenic regions are highlighted. CGI = CpG island. **e**. (Left) Representative stochastic optical reconstruction microscopy (STORM) images of the indicated cell lines stained for Histone 3. (Right) STORM quantifications of percentage clustered (top), median cluster area (middle), and median points per cluster (bottom) of H3. Data are represented as mean ± standard deviation.

data point to a role for PRC2 in regulating global compaction and implicate global chromatin decompaction in the aetiology of Weaver syndrome.

An EZH2 variant associated with a growth restriction disorder confers opposite chromatin defects

The A733T EZH2 SET domain variant associated with the opposing growth restriction disorder (Fig. 5a) exhibits increased histone methyltransferase activity *in vitro* [26]. We wished to determine the consequences of this potential gain-of-function EZH2 variant on the genome-wide deposition of H3K27me2 and H3K27me3. To this end, we expressed either wild-type EZH2, the growth-restriction-associated EZH2-A733T variant, or the Weaver syndrome-associated EZH2-Y728* variant in *Ezh2*$^{fl/\Delta}$ heterozygous mouse ESCs and performed immunoblot analyses (Fig. 5b). These revealed that the EZH2-A733T variant caused stark global increases in H3K27me3, coupled with global reductions in H3K27me1, H3K27me2, and H3K27ac (Fig. 5b).

Next, we performed ChIP-Rx of H3K27me2, H3K27me3, and H3K27ac on *Ezh2*$^{fl/\Delta}$ heterozygous mouse ESCs expressing either wild-type EZH2, the growth restriction-associated EZH2-A733T variant, or the Weaver syndrome-associated EZH2-Y728* or EZH2-A677T variant. In direct contrast to the Weaver syndrome-associated EZH2 variants, the growth restriction EZH2-A733T variant caused genome-wide and intergenic increases of H3K27me3 coupled with decreased H3K27ac (Fig. 5c and Extended Data Fig. 4a-b). In ChIP-Rx tracks, we observed high levels of H3K27me3 spreading pervasively from PRC2 bound sites into surrounding intergenic regions in the EZH2-A733T variant cell line, and associated with reciprocal H3K27ac losses (Figure 5d). Generally, the genome-wide gains in H3K27me3 occurred where H3K27ac was lost, and H3K27me2 was also lost from these same regions as it was converted to H3K27me3 (Fig. 5e and Extended Data Fig. 4c). Taken together, these data suggest that global H3K27 hyper-trimethylation and H3K27 hypo-acetylation are linked with the growth restriction-associated EZH2 variant, and *vice versa* for Weaver Syndrome overgrowth associated EZH2 variants (Fig. 5f). Importantly, given that these intergenic chromatin changes are directly opposing between Weaver syndrome and growth restriction-associated EZH2 variants, this lends support to their potential biological relevance in the opposing developmental phenotypes.

Opposing chromatin and transcriptional effects between Weaver syndrome and growth restriction-associated EZH2 variants

We next wanted to compare the effects of the growth restriction-associated EZH2-A733T variant against the Weaver syndrome-associated EZH2 variants on the chromatin and transcriptional state of Polycomb target genes. ChIP-Rx analyses revealed that expression of EZH2-A733T increased levels of H3K27me3 at PRC2 target gene promoters, and this was associated with reduced H3K27me2 – reflecting the gain-of-function nature of this EZH2 variant (Fig. 6a). We next performed RNA-seq to analyse RNA transcript abundance in *Ezh2*$^{fl\Delta}$ heterozygotes expressing either wild-type EZH2 or Weaver syndrome-associated EZH2 variants. Expression of Weaver syndrome-associated EZH2 variants led to higher numbers of differentially abundant genes compared to the *Ezh2*$^{fl\Delta}$ heterozygote, again implying dominant-negative effects of Weaver syndrome-associated EZH2 variants on transcriptional regulation (Fig. 6b). 18 of these genes had increased RNA abundance across at least 4 of the 5 Weaver syndrome-associated EZH2 variant-expressing cell lines (Fig. 6C and Extended Data Fig. 5a-b). Importantly, these upregulated genes are Polycomb targets and were conversely downregulated in the growth restriction-associated EZH2-A733T- expressing cells (Fig. 6d). Interestingly, some of these genes (*Akt3*, *Meis2*, *Gja1* and *Pbx1)* are associated with human developmental disorders exhibiting aberrant growth phenotypes[34–39], and mutations in others (*Adam23* and *Zfp521*) are associated with aberrant growth phenotypes in mice[40,41].

All 18 of these genes are all normally bound by PRC2 (SUZ12) and cPRC1 (CBX7), and enriched for H3K27me3 in ESCs (Fig. 6e). These genes tended to lose enrichment of SUZ12, CBX7, and H3K27me3 when Weaver syndrome-associated EZH2 variants were expressed (Fig. 6e and Extended Data Fig. 5c). Despite having increased H3K27me3 on most Polycomb target genes, the EZH2-A677T Weaver syndrome-associated variant also tended to have reduced H3K27me3 and CBX7 at this specific cohort of 18 sensitive Polycomb target genes (Fig. 6e and Extended Data Fig. 5c). By contrast, the growth restriction-associated EZH2-A733T variant caused increased H3K27me3, SUZ12, and CBX7 enrichment at these genes (Fig. 6e and Extended Data Fig. 5c). Strikingly, the strong changes in SUZ12, CBX7, and H3K27me3 enrichments were not a general feature of all Polycomb target genes, but were observed at this cohort of 18 transcriptionally dysregulated Polycomb target genes. For example, the *Vim*, *Gja1*, and *Akt3* genes had strongly decreased H3K27me3, SUZ12 and CBX7 ChIP-Rx enrichments in cells expressing WS variants, but increased enrichments in cells expressing the growth restriction variant (Fig. 6e and Extended Data Fig 5c). In contrast, the majority of other Polycomb bound genes (e.g. *Bmp2, Atf3*, and *Cnr1)* were not transcriptionally dysregulated and did not have strong H3K27me3, SUZ12 or CBX7 changes at their gene promoters in any of the *Ezh2*$^{fl\Delta}$ heterozygote ESCs

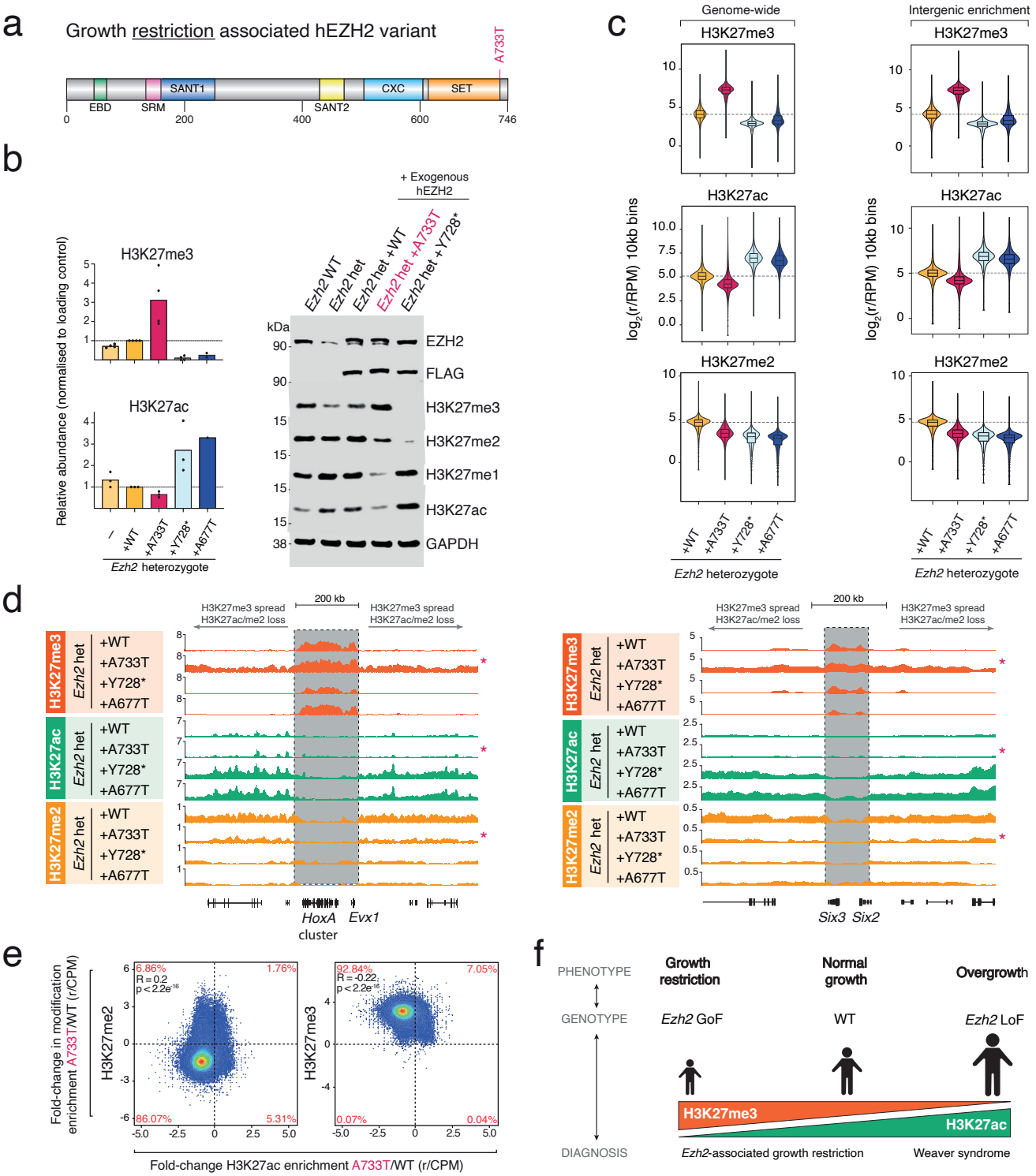

Figure 5. An EZH2 mutation associated with growth restriction induces opposing histone modification changes. a. Schematic of the human EZH2 protein showing the location of the A733T growth restriction-associated mutation. **b.** (Left) Relative quantification of immunoblot analyses of H3K27me3 (top) and H3K27ac (bottom) abundance in the indicated cell lines. Data values represent independent biological replicates, and their mean values are plotted as bars. (Right) Representative immunoblots for FLAG, EZH2, and H3K27 modification states, probing whole cell lysates from the indicated cell lines. GAPDH is shown as a loading control. **c.** Violin plot representations of the log2 ChIP-Rx normalized reads per million (r/RPM) of H3K27me3, H3K27ac and H3K27me2 enrichments in the indicated cell lines genome-wide (left) and across 188,538 10kb bins representing all intergenic regions (right). Dashed lines represent the Ezh2$^{fl/\Delta}$ + EZH2-WT values. **d.** UCSC genome browser tracks showing ChIP-Rx normalised reads of H3K27me3, H3K27ac and H3K27me2 at the *HoxA* gene cluster (left) and *Six2/3* genes (right) in the indicated cell lines. **e.** Correlation plots demonstrating the relationship between changes in genome-wide ChIP-Rx enrichment of H3K27me2 (left) or H3K27me3 (right) and H3K27ac in the EZH2-A733T growth restriction variant compared to EZH2-WT. The percentage of 10kb bins in each quadrant is indicated. The p-value and correlation coefficient were calculated using Pearson's correlation. **f.** Schematic illustrating a proposed model for the roles of H3K27 methylation and acetylation levels in controlling human growth during development.

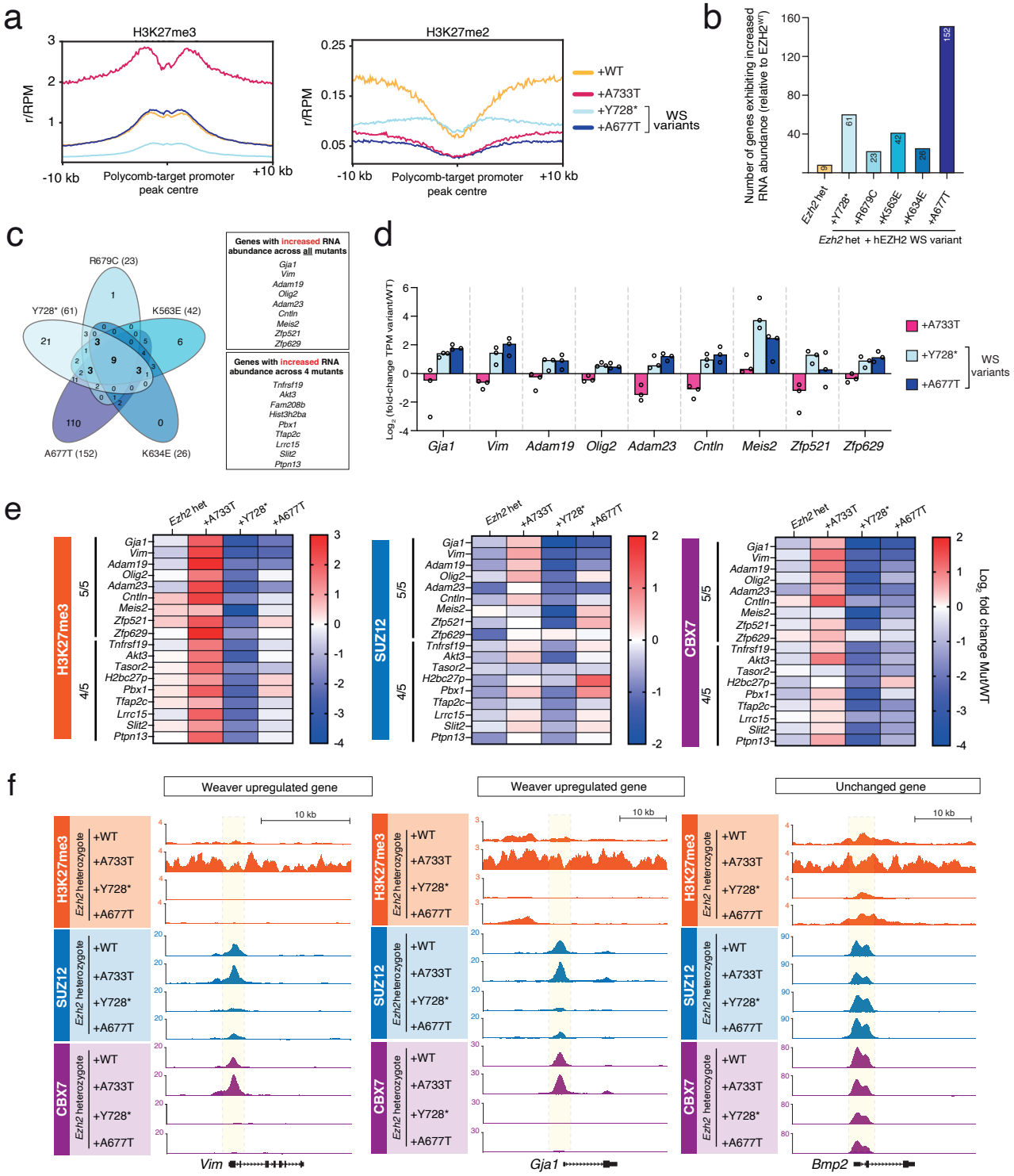

Figure 6. The growth restriction-associated EZH2 variant causes opposite chromatin and transcriptional changes at Polycomb target genes compared to Weaver Syndrome EZH2 variants. a. Average ChIP-Rx signal profiles for H3K27me3 and H3K27me2 at Polycomb target promoters (n = 3870) in the indicated cell lines. **b.** Bar chart representing the total number of genes whose RNA transcripts significantly (≥1.5 fold) increased in abundance in the indicated cell lines compared to the EZH2-WT rescue cell line. **c.** Venn diagram presenting the numbers and overlap of genes increased in RNA abundance in the indicated WS variant expressing cell lines. (Right) List of genes specifically increased in at least 4 WS variant cell lines. **d.** Bar plots showing the log2 fold change in RNA abundance of the named genes in the indicated cell lines, relative to the EZH2-WT rescue. Data points represent TPM values from biologically independent RNA-seq experiments and median values are plotted as bars. **e.** Heatmaps representing the log2 fold change in ChIP-Rx enrichment of H3K27me3, SUZ12 and CBX7 at the genes listed upregulated in cells expressing growth restriction or Weaver syndrome variant EZH2 compared to EZH2-WT rescue cell line. **f.** UCSC genome browser tracks showing ChIP-Rx normalised reads of H3K27me3, SUZ12 and CBX7 in the indicated cell lines at two genes increased in RNA abundance in WS-associated variant cell lines (*Vim, Gja1*); note that ChIP-Rx signal is lost from the WS variant cell lines but gained in the growth restriction variant cell line. For comparison, a Polycomb target gene which did not change in RNA abundance (*Bmp2*) is also shown.

.

expressing Weaver syndrome-associated EZH2 variants (Fig. 6f and Extended Data Fig. 5c). Taken together, these data support opposing transcriptional dysregulation and H3K27 modification states at a specific cohort of vulnerable Polycomb genes, coupled with alterations in the intergenic chromatin state, as being central to the aetiologies of EZH2-associated aberrant growth phenotypes.

Discussion

Here we present an investigation of the chromatin and transcriptional effects of a broad range of EZH2 variants associated with Weaver overgrowth syndrome, as well as an opposing EZH2 variant that causes a growth restriction syndrome. We provide the first evidence that Weaver associated EZH2 mutations confer dominant negative effects on the global H3K27 methylation activities of PRC2. These dominant negative effects impact H3K27me2 deposition at intergenic regions of the genome, along with H3K27me3 deposition and cPRC1 binding at a select cohort of sensitive Polycomb target genes. Strikingly, we observed directly opposing effects for an EZH2 variant associated with a growth restriction syndrome. We propose that these opposing chromatin and transcriptional defects are central to the underlying pathophysiology of EZH2-related growth disorders.

Weaver syndrome-associated EZH2 variants dominant negatively affect PRC2 activity

We discovered that Weaver syndrome-associated EZH2 mutations confer dominant negative effects on PRC2 functions. Global levels of H3K27me2/3 were lower in cells expressing the Weaver syndrome-associated EZH2 variants compared to the *Ezh2* heterozygous ESCs, indicating that they negatively interfere with the function of wild-type EZH2 in cells. Interestingly, these dominant negative effects were not observed at all Polycomb target genes across all variants; one variant (EZH2-A677T) exhibited increased H3K27me3 at most, though not all, Polycomb target genes. Cells expressing Weaver syndrome-associated EZH2 variants also exhibited more transcriptional dysregulation than heterozygous knockouts, and we observed dominant negative effects on the loss of cPRC1 and PRC2 binding at the Polycomb target genes consistently upregulated in WS variant expressing cell lines. We therefore propose that dominant negative effects are a central mutational mechanism in Weaver syndrome.

Our discovery of dominant negative effects of WS EZH2 variants can explain the absence of early truncating mutations in the *EZH2* gene in Weaver syndrome cases reported to date. Such early truncating mutations would be predicted to lead to nonsense-mediated decay of the transcribed mutant mRNA after a premature stop codon, and ultimately result in the expression of only the one wild-type allele of EZH2 at the protein level. Perhaps this simple haploinsufficiency would not sufficiently impair PRC2 activity to produce a Weaver syndrome phenotype. It is possible that EZH1 may be able to partially compensate for heterozygous loss of EZH2 activity. Although EZH1 catalytic activity is significantly lower than EZH2, and its expression is 20-fold lower in ESCs[14], it might become prominent at later stages of development where its expression levels are increased. In contrast to Weaver syndrome-associated *EZH2* mutations, IMMAS-associated *SUZ12* mutations do include premature termination codon mutations, presumably resulting in nonsense-mediated decay and haploinsufficiency of the SUZ12 protein[16]. Loss of SUZ12 would affect PRC2 complexes containing both EZH2 and EZH1, supporting the possible EZH1 compensatory mechanism for EZH2 premature termination codon mutations. The exact mechanism(s) through which these Weaver syndrome-associated EZH2 dominant negative effects are conferred will be an important subject for further investigation.

Weaver syndrome mutations overlap with cancer-associated EZH2 mutations

Individuals with Weaver syndrome are highly predisposed to developing cancers[42]. Indeed, some Weaver syndrome mutations are directly found in cancer malignancies, including EZH2-R679C (variant 1) and EZH2-Y728* (variant 9)[43]. Here, we characterize the Weaver syndrome-associated EZH2-A677T variant and find that it acts similarly to 'gain-of-function' EZH2 variants causative of B-cell lymphoma [30]. Our data are consistent with it having an enhanced ability to convert H3K27me2 to H3K27me3. Notably, the individual with Weaver syndrome caused by this A677T mutation developed both neuroblastoma and acute lymphoblastic leukemia at 13 months old[21]. Interestingly, *MEIS2,* one of the genes upregulated in the presence of Weaver syndrome-associated EZH2 variants, is a Polycomb target gene encoding a transcription factor expressed in the developing brain and associated with neuroblastoma, a cancer which disproportionately affects children with Weaver syndrome [44,45]. *PBX1*, another gene in the upregulated cohort, is known to dimerise with MEIS transcription factors, functionally linking these two upregulated genes to each other and to cancer[46].

Taken together, we propose that cellular assays coupled with genomic profiling of H3K27 modifications may represent a useful means to predict cancer predisposition in individuals with Weaver syndrome.

Transcriptional dysregulation of a small cohort of relevant growth-associated genes

We identified a cohort of 18 Polycomb target genes that were consistently derepressed by Weaver syndrome-associated EZH2 mutations. Interestingly, many of these dysregulated genes are themselves implicated in growth phenotypes or disorders. For example, activating mutations in *AKT3* are associated with a human disorder featuring macrocephaly and overgrowth[35,39,47], and this gene is differentially methylated in cells taken from individuals with Weaver Syndrome[26]. AKT3 is a protein kinase expressed during human neurogenesis and part of the mTOR pathway which is central to cell growth[48,49]. Furthermore, inactivating mutations in several of the upregulated genes cause human disorders associated with short stature or growth delay, including *GJA1*[38,50], *MEIS2*[34], and *PBX1*[36,37]. Mice with inactivating mutations in 3 upregulated genes result in smaller body size or other growth defects, including *Adam23*[40], *Zfp521*[41], and *Akt3*[51]. Furthermore, in the Mouse Genome Database, a "growth/size/body" phenotype related to reduced growth is listed for mice with inactivating mutations in the *Meis2*, *Zfp52*, *Gja1*, *Zfp629*, *Pbx1* and *Tfap2c* genes[52]. Additionally, overexpression of some of these genes is associated with non-growth related Weaver syndrome phenotypes. For example, overexpression of *Zfp521* causes increased bone formation in mice[53], while overexpression of *OLIG2* is associated with the cognitive deficits observed in Down Syndrome[54–56].

Notably, although it is likely that the opposing chromatin changes observed between overgrowth and growth restriction-associated EZH2 variants will be conserved across many cell types, the specific genes that are transcriptionally dysregulated may vary across cell types due to specific localization of the chromatin defects and the availability of cell type-specific transcription factors. Therefore, much can be learned from studying these EZH2 variants in additional lineage-specific contexts such as chondrocyte, neural stem cell or lymphoblastoid cell lines, or during differentiation, where the effects of the mutations may be more pronounced.

The general utility of monitoring the genome-wide consequences of growth syndromes associated with mutations of epigenetic enzymes

We show that Weaver syndrome-associated EZH2 variants cause varying degrees of dominant-negative impairment of PRC2 functions which correlates with the phenotype. Consistent with the variable clinical presentation of Weaver syndrome[23–25], we observed that the level of functional impairment of PRC2 histone methylation activity varied across different WS mutations, from mild to severe. For example, we identified one mutation of *EZH2* reported to be associated with a case of Weaver syndrome (EZH2-D233V) that did not impair the global histone methylation activities of PRC2. However, we note that the individuals diagnosed with Weaver syndrome who had this mutation had relatively mild clinical presentations, in line with the lack of cellular effects[21]. In contrast, the EZH2 variant Y728* was the most severely impaired in terms of its histone methyltransferase activity in our cellular assays and the individual with this variant had notably strong clinical presentations of Weaver syndrome, particularly in terms of increased height[20]. This concurrence with actual WS clinical presentations supports the validity and usefulness of our cellular assay.

Therefore, we propose that the cellular assay and investigative strategy designed here could be extended to study other growth disorders caused by mutations in chromatin regulators, such as *SUZ12*, *EED*, *ASXL1-3*, *NSD1*, *DNMT3a*, *CHD8*, *ARID1B*, *BRM*, and *CBP/EP300*[35,57–59]. Notably, loss-of-function mutations in CBP/P300 H3K27 acetyltransferases cause Rubinstein-Taybi syndrome, which is characterized by short stature, microcephaly and other features directly opposing Weaver syndrome clinical presentation[57]. It is possible that the defects in H3K27 acetyltransferase activity could lead to lower levels of H3K27ac across the genome, similar to the effects of the growth restriction-associated EZH2 variant studied here, and in contrast to the elevated levels of H3K27ac observed in our cells expressing Weaver syndrome-associated variants.

In summary, we have shown here that cellular modelling of mutations to identify common changes across overgrowth syndromes, and directly opposing changes in growth restriction models, is a powerful way to pinpoint cellular defects that are central to these disorders.

Methods

Cell Culture and cell lines

Mouse embryonic stem cells (ESCs) were grown on 0.1% gelatin-coated culture dishes in Glasgow Minimum Essential Medium (Sigma) supplemented with 20% (v/v) heat-inactivated FBS (Gibco), 100 U/mL Penicillin and 100 μg/mL Streptomycin (Gibco), 50 μM β-mercaptoethanol, 1:100 GlutaMAX (Gibco), 1:100 non-essential amino acids (Gibco), 1 mM sodium pyruvate (Gibco), 1:500 leukaemia inhibitory factor (LIF; produced in-house), 3 μM CHIR99021 (Cayman Chemical Company) and 1 μM PD0325901 (Cayman Chemical Company). HEK293T cells (for lentivirus production) and NTERA-2 cells (for ChIP-Rx spike-in) were grown on TC-treated culture dishes in high glucose Dulbecco's Modified Eagle's Medium (Sigma) supplemented with 10% (v/v) FBS (Gibco), 100 U/mL Penicillin and 100 μg/mL Streptomycin (Gibco).

The heterozygous *Ezh2* knockout cell line was generated by treating the *Ezh2*$^{fl/fl}$;*Rosa26CreERT2* ESCs with 0.5 μM 4-OHT for 12 hours. Single cells were from this population were then sorted into 96-well culture plates using a FACSAria Fusion Flow Cytometer. Individual clones were screened at the gDNA level for the desired heterozygous deletion in Ezh2, and positive clonal populations were expanded for further validation at the mRNA and protein expression level.

Stable cell lines expressing exogenous hEZH2 constructs were generated by lentiviral transduction. A second-generation lentiviral system was used to produce lentivirus particles in HEK293T cultures. ESCs were seeded at a density of ~2×10^4 cells per cm^2 on day 0, then treated with virus on day 1 and day 2. Approximately 48 hours post-transduction, cells were washed with DPBS and treated with 1 μg/mL puromycin. Antibiotic selection was maintained for an empirically defined length of time (typically four to six days) to obtain putative stable cell lines, which were subsequently screened for expression of the intended transgene.

Plasmids

Human EZH2 expression vectors were generated using Gateway cloning and the in-house pLENTI-EFIA-FLAG/HA lentiviral expression vector[60]. Mutant hEZH2 ORFs were generated by Q5 Site-Directed Mutagenesis (NEB E0554S) as per the manufacturer's protocol. Note that our hEZH2 ORF corresponds to EZH2 isoform 1 (Q15910-1, 746 amino acids).

Immunoblotting

Whole-cell protein samples were prepared in ice cold High Salt buffer (50 mM Tris-HCl pH 7.2, 300 mM NaCl, 0.5% (v/v) NP-40, 1mM EDTA pH 7.4, 2 μg/mL aprotinin, 1 μg/mL leupeptin, 1mM PMSF). Cell suspensions were sonicated and then rotated at 4 °C for 20 minutes to ensure sufficient lysis. Lysates were next clarified by centrifugation at ≥ 20,000 RCF at 4°C for 20 minutes. Normalised protein lysates were denatured and separated on Bolt Bis-Tris (Invitrogen) or NuPAGE Bis-Tris (Invitrogen) gels, then transferred to nitrocellulose membranes (0.2 μM, Amersham). Membranes were blocked against nonspecific binding and then incubated with the relevant primary (overnight at 4 °C) and secondary (1h at RT) antibodies. Relative protein levels were determined by chemiluminescence or infrared fluorescence detection on a LI-COR Odessy Fc. For details on the antibodies used, see Table 2.

STORM imaging and analysis

For STORM imaging, 35m MMATTEK (P35G-1.5-14-C) plates were gelatinised with 0.1% gelatin. 500,000 ESC were seeded per plate for 20-22 h before 6 minutes fixation in 1:1 Methanol: Ethanol at -20°C. Samples were blocked in blocking buffer (PBS with 10% donkey serum) for one hour at room temperature. Samples were incubated overnight at 4°C with H3 antibody (ab1791) 1:70 dilution in blocking buffer + 0.1% Triton X-100. Samples were incubated in 1:200 dilution of Alexafluor-647 secondary antibody in PBS in the dark for one hour at room temperature. Samples were then post-fixed in 2% PFA for 5 minutes before storing in PBS at 4°C until imaging. Direct STORM (dSTORM) imaging was performed using the Nikon N-STORM microscope equipped with a 1.49 NA CFI Apochromat TIRF objective, exciting the Alexa Fluor 647 dye with the 647 nm laser light in HILO (highly inclined and laminated optical sheet) mode[61]. The 405 nm laser light (activation laser) was used for reactivating the Alexa Fluor 647 into a fluorescent state. The activation laser power was automatically increased by the NIS software to keep the number of localizations per frame constant up to a maximum of 50% of the laser power. Each dSTORM acquisition consisted of 40 thousand images recorded with an Orca-Flash4.0 sCMOS camera (Hamamatsu) with an exposure time of 20 ms, a pixel size of 161.5 nm and a field of view of 128x128 pixels. During dSTORM acquisitions, cells were kept in imaging buffer (100 mM MEA, 1% glucose, 560 ug/mL Glucose Oxidase and 34 ug/mL Catalase in PBS). Two regions of interest (ROI) of 32x32 pixels for each dSTORM image were processed using ThunderSTORM [62], with a pre-detection wavelet filter (B-spline, scale 2, order 3), initial detection by non-maximum suppression (radius 1, threshold at one standard deviation of the F1 wavelet), and sub-pixel localization by integrated Gaussian point-spread function and maximum likelihood estimator with a fitting radius of 3 pixels. Detected localizations were filtered (intensity > 500 photons, sigma range of 50–500, and localization uncertainty < 20 nm). The filtered dataset was then corrected for sample drift (cross-correlation of images from five bins at a magnification of 5) and repeated localizations was removed by merging points which reappeared within 20 nm. STORM images were visualized using the normalized Gaussian method with a lateral uncertainty of 20 nm. Cluster analysis were performed thanks to a supervised machine learning approach using trained neural network (Williamson et al., 2020). The CAML (Cluster Analysis by Machine Learning) analysis workflow consisting of 3 stages and corresponding Python scripts, was used to: 1) prepare the data converting the x,y localization tables in a list of near-neighbor distances; 2) evaluate the input data with a trained model; 3) extract clustering information. The 87B144 model was used [63], considering the possibility that more than 100 localizations per cluster could occur in our dataset.

RNA-seq

Total RNA was isolated from cells using the RNeasy Mini Kit (Qiagen; 74106) as per the manufacturer's protocol. The quality of extracted RNA was confirmed using the TapeStation (Agilent) with the RNA ScreenTape assay reagents (Agilent; 5067-5576). For each sample, 1 µg of high-quality RNA (RIN ≥ 8.0) was used as input material for library preparation. RNA-seq libraries were prepared in accordance with the manufacturer's instructions, using the NEBNext rRNA Depletion Kit v2 (Human/Mouse/Rat) (NEB E7405) or the NEBNext Poly(A) mRNA Magnetic Isolation Module (NEB E7490), followed by the NEBNext Ultra II RNA Library Prep Kit for Illumina (NEB E7770). Library DNA was quantified using the Qubit, and size distributions were ascertained on a TapeStation (Agilent) using the D1000 ScreenTape assay reagents (Agilent; 5067-5583). This information was used to calculate pooling ratios for multiplex library sequencing. Pooled libraries were diluted and processed for 35-bp paired-end sequencing on an Illumina NextSeq 500 instrument (ID: NB501524) using the NextSeq 500 High Output v2 kit (75 cycles) (Illumina; FC-404-2005) in accordance with the manufacturer's instructions.

Quantitative ChIP

Cells were counted and normalized cell pellets (each of equal cell number, up to 50×10^6) were washed twice with DPBS before crosslinking for 10 minutes with 1% formaldehyde (Sigma) in DBPS. Crosslinking was quenched with 125 mM glycine for 5 minutes, followed by two PBS washes. Crosslinked cells were lysed in an appropriate volume of SDS-lysis buffer (100 mM NaCl, 50 mM Tris pH 8.1, 5 mM EDTA pH 8.0, 0.5% SDS, 2 µg/mL aprotinin, 1 µg/mL leupeptin, 1 mM PMSF). Chromatin was pelleted by centrifugation at 350 RCF for 5 minutes at room temperature. The supernatants were discarded, and chromatin resuspended in ChIP buffer (2:1 dilution of SDS-lysis buffer/Triton dilution buffer [100 mM Tris pH 8.6, 100 mM NaCl, 5 mM EDTA pH 8.0, 5% Triton X-100, 2 µg/mL aprotinin, 1 µg/mL leupeptin, 1 mM PMSF]). For quantitative ChIP analyses (ChIP-Rx), spike-in chromatin was prepared from NTERA-2 cells and added to ESC samples (1:10 cell number ratio) at this point in the preparation procedure.

Chromatin samples were sheared using a Branson Sfx150 Sonifier for a total sonication time of 4-5 min at 50% power and a duty cycle of 1 s on and 4 s off. ChIPs were performed overnight at 4 °C. For details on the antibodies used, see below. To ChIP FLAG-tagged proteins, sonicated chromatin was instead incubated overnight with 40 µL equilibrated anti-FLAG beads (gift from Dr. Claudio Ciferri). For all other ChIPs, following overnight incubation each sample received 40 µl of Protein G Dynabeads and was incubated for a further 3 h at 4 °C. Beads were washed three times in mixed micelle buffer (150 mM NaCl, 20 mM Tris pH 8.1, 5 mM EDTA pH 8.0, 5.2% Sucrose, 1% Triton X-100, 0.2% SDS), twice with buffer 500 (0.1% Sodium Deoxycholate, 1 mM EDTA pH 8.0, 50 mM HEPES pH7.5, 1% Triton X-100), twice with LiCl detergent wash (0.5% Sodium Deoxycholate, 1 mM EDTA pH 8.0, 250 mM LiCl, 0.5% NP-40, 10 mM Tris pH 8.0) and once wash with TE (10 mM Tris pH 8.0, 1 mM EDTA pH 8.0). Samples were eluted from beads using elution buffer (0.1 M NaHCO3, 1% SDS) while shaking for 1 h at 65 °C, then supernatants were incubated overnight at 65°C to reverse crosslinking. Enriched DNA fragments were Rnase (Thermo Fisher) and Proteinase K (Sigma) treated prior to purification using Qiagen MinElute PCR Purification Kit (Qiagen; 28006).

ChIP library preparation. ChIP-purified DNA was quantified by fluorimetry using the Qubit dsDNA High Sensitivity Assay Kit (Thermo Fisher), and 0.5–50 ng of DNA/ChIP was used for library preparation using the NEBNext Ultra II DNA Library Kit for Illumina (NEB E7645) and NEBNext Multiplex Oligos for Illumina (Index Primers Set 1 and 2; NEB E7335 and E7500). Library DNA was quantified using the Qubit, and size distributions were ascertained on a TapeStation (Agilent) using the D1000 ScreenTape assay reagents (Agilent; 5067- 5583). This information was used to calculate pooling ratios for multiplex library sequencing. Pooled libraries were diluted and processed for either 75-bp single-end or 35-bp paired-end sequencing on an Illumina NextSeq 500 instrument (ID: NB501524) using the NextSeq 500 High Output v2 kit (75 cycles) (Illumina; FC-404-2005) in accordance with the manufacturer's instructions.

ChIP-Rx data analysis

Chromosome names for the human genome were modified with the prefix hg38_ and a metagenome was created by concatenating the mouse and human reference genomes (mm10 and hg38, respectively) before indexing with Bowtie 2 (version 2.3.5[64], as described[65]). Reads were aligned to the metagenome using Bowtie 2 with default parameters, with the exception of –no-unal. Non-unique read alignments were filtered out using SAMtools (version 1.10; [66]) to exclude those with an alignment quality of <2, and the hg38_ prefix appended to chromosome names was used to separate reads as aligned to the reference mouse or spike-in human genomes. SAMtools was used to convert SAM files to BAM files and to remove duplicate aligned reads. Spike-in normalization factors were calculated for each ChIP using the formula for normalized reference-adjusted reads per

million (RRPM) as described [65], (1 per million spike-in reads). BigWig files were generated using the bamCoverage tool from the deepTools suite (version 3.5.0; Ramírez et al., 2016) with a bin size of 10 and scaled using the RRPM normalization factor derived for each sample. BAM files were converted to BED format using the bamToBed function in BEDTools (version 2.27.1; [68]) and used for peak calling with HOMER (version 4.10; [69]), using BED files from input ChIP-Rx as a control. The computeMatrix function in deepTools was used to score the coverage of BigWigs in genomic regions of interest prior to generating average and tornado plots using the plotProfile and plotHeatmap functions respectively. The featureCounts program version 1.6.4 was used to calculate the average ChIP signal at the TSS of genes of interest from the BAM files. The average signals were multiplied by the spike-in normalisation factors and heatmaps were generated using the Graphpad software (version 9.5.1).

The mm10 reference genome was split into 10-kb windows using the makewindows function in BEDTools, and regions in the ENCODE mm10 blacklist were removed using bedtools intersect with the -v and -wa flags [70]. BEDTools coverage was used to summarize overlapping read alignments in BAM files within these bins and scaled using RRPM normalization. Resulting counts were used for the generation of chromosome-wide-coverage line graphs and XY density scatter plots.

Promoter regions were identified by taking −1,500 bases upstream and +600 bases downstream of annotated transcription start sites in the Ensembl 98 mm10 genome annotation. PRC target promoters were defined by overlapping SUZ12 and CBX7 peak sets with gene promoter regions defined within the mm10 build of the mouse genome. Gene body regions were defined by taking the gene annotations as defined in the Ensembl 98 mm10 genome annotation and converted to the bed format using a custom script. The BEDTools complement tool was used to generate a BED file of intergenic regions by supplying the gene body BED file a FASTA index of the mm10 genome as input (generated using SAMtools faidx).

RNA-seq data analysis

RNA-seq reads were pre-processed to remove the universal Illumina sequencing adapter 'AGATCGGAAGAG' using cutadapt (version 3.2; Martin, 2011). The STAR (version 2.7.3a; [72]) algorithm was used to align reads to the mouse reference genome (mm10) in two-pass mode, enabling the identification of novel splice junctions during alignment. SAM files were converted to sorted BAM files using SAMtools (version 1.10). Read alignments were assigned to gene identifier features annotated in the Ensembl 98 mm10 genome annotation using featureCounts (version 1.6.4[73]). The DESeq2 R package (version 1.24.0[74]) was utilized to identify differentially abundant transcripts at a fold change of >1.5 with a baseMean expression of >20 and a Benjamini–Hochberg-adjusted P value of <0.05. Batch effects were reduced by the inclusion of the formula "~ batch + mutation status" to the design of the linear model.

In silico mutagenesis and structural modelling

In silico mutagenesis was carried out in the context of the structure of PRC2.2 with a substrate nucleosome (PDB 6WKR). In silico mutagenesis was carried out using PyMol and van der Waals clashes between the mutated amino acids to residues in their vicinity were visualised using the show_bumps script, with clashes represented by discs. Red discs represent severe clashes and their diameter increases with clashes severity. Green discs represent nearly clashes. In cases where more than one rotamer was possible, the rotamer that provides the least severe clashes is presented.

Acknowledgements

We thank members of the Bracken lab for helpful discussions and critical reading of the manuscript. We are grateful to the Genomics Core at University College Dublin for expertise and help with next-generation sequencing. We thank Kristian Helin for providing the *Ezh2*$^{fl/fl}$ and *Ezh1/2* dKO cell lines. Work in the Bracken lab is supported by the Irish Research Council Advanced Laureate Award (IRCLA/2019/21) and Science Foundation Ireland (SFI), under the SFI Investigators program (SFI/16/IA/4562), the Irish Cancer Society (CancersUnmetNeeds012) and the St. Vincent's Foundation. O.D. was supported by a PhD fellowship from the Irish Research Council Government of Ireland Postgraduate Scholarship Programme (GOIPG/2017/2009). E.T. was supported by a PhD fellowship from the Irish Research Council Government of Ireland Postgraduate Scholarship Programme (GOIPG/2019/3481). F.M. was supported by a PhD fellowship from Trinity College Dublin Provost Award. E.C was supported by an SFI/IRC Pathway Program grant (21/PATH-S/9384) and a Wellcome Trust Early Career Award [225152/Z/22/Z]. The work of the Pasini laboratory was supported by the World Wide Cancer Research (22-0027); the Italian Association for Cancer Research, AIRC (IG-2017-20290 and IG 2022-27694); and by the European Research Council, ERC (EC-H2020-ERC-CoG-DissectPcG: 725268).

Author Contributions

O.D. and A.P.B. conceived of the project and designed the experiments. O.D. engineered the EZH2-variant ESC cultures and performed most of the bench-based experiments. F.M. performed additional Western blot and ChIP-Rx experiments. C.M. and F.M. performed the bioinformatics analyses. E.C. and S.R. performed STORM imaging experiments and analysis. Q.Z. and C.D. performed and interpreted the structural modelling of variant EZH2 proteins. O.D., E.T. and A.P.B. co-wrote the manuscript with contributions from all other authors.

Competing Interests statement

The authors declare no competing interests.

References

1. Schuettengruber, B., Bourbon, H. M., Di Croce, L. & Cavalli, G. Genome Regulation by Polycomb and Trithorax: 70 Years and Counting. *Cell* **171**, 34–57 (2017).

2. Margueron, R. & Reinberg, D. The Polycomb complex PRC2 and its mark in life. *Nature* **469**, 343–349 (2011).

3. Laugesen, A., Højfeldt, J. W. & Helin, K. Molecular Mechanisms Directing PRC2 Recruitment and H3K27 Methylation. *Mol. Cell* **74**, 8–18 (2019).

4. Glancy, E., Ciferri, C. & Bracken, A. P. Structural basis for PRC2 engagement with chromatin. *Current Opinion in Structural Biology* **67**, 135–144 (2021).

5. Deevy, O. & Bracken, A. P. PRC2 functions in development and congenital disorders. *Development* **146**, dev181354 (2019).

6. Bracken, A. P., Dietrich, N., Pasini, D., Hansen, K. H. & Helin, K. Genome-wide mapping of polycomb target genes unravels their roles in cell fate transitions. *Genes Dev.* **20**, 1123–1136 (2006).

7. Boyer, L. A. *et al.* Polycomb complexes repress developmental regulators in murine embryonic stem cells. *Nature* **441**, 349–353 (2006).

8. Lee, T. I. *et al.* Control of developmental regulators by Polycomb in human embryonic stem cells. *Cell* **125**, 301–313 (2006).

9. Bracken, A. P., Brien, G. L. & Verrijzer, C. P. Dangerous liaisons: interplay between SWI/SNF, NuRD, and Polycomb in chromatin regulation and cancer. *Genes Dev.* **33**, 936–959 (2019).

10. Glancy, E. *et al.* PRC2.1- and PRC2.2-specific accessory proteins drive recruitment of different forms of canonical PRC1. *Mol. Cell* (2023). doi:10.1016/J.MOLCEL.2023.03.018

11. Ferrari, K. J. *et al.* Polycomb-Dependent H3K27me1 and H3K27me2 Regulate Active Transcription and Enhancer Fidelity. *Mol. Cell* **53**, 49–62 (2014).

12. Lee, H. G., Kahn, T. G., Simcox, A., Schwartz, Y. B. & Pirrotta, V. Genome-wide activities of Polycomb complexes control pervasive transcription. *Genome Res.* **25**, 1170–1181 (2015).

13. Conway, E., Healy, E. & Bracken, A. P. PRC2 mediated H3K27 methylations in cellular identity and cancer. *Curr. Opin. Cell Biol.* **37**, 42–48 (2015).

14. Streubel, G., Watson, A., Krogan, N. J., Bracken, A. P. & Cagney, G. The H3K36me2 Methyltransferase Nsd1 Demarcates PRC2-Mediated H3K27me2 and H3K27me3 Domains in Embryonic Stem Cells. *Mol. Cell* **70**, 371-379.e5 (2018).

15. Cyrus, S., Burkardt, D., Weaver, D. D. & Gibson, W. T. PRC2-complex related dysfunction in overgrowth syndromes: A review of EZH2, EED, and SUZ12 and their syndromic phenotypes. *Am. J. Med. Genet. Part C Semin. Med. Genet.* **181**, 519–531 (2019).

16. Cyrus, S. S. *et al.* Rare SUZ12 variants commonly cause an overgrowth phenotype. *Am. J. Med. Genet. Part C Semin. Med. Genet.* **181**, 532–547 (2019).

17. Hetzelt, K. L. M. L. *et al.* Manifestation of epilepsy in a patient with EED -related overgrowth (Cohen–Gibson syndrome). *Am. J. Med. Genet. Part A* (2021). doi:10.1002/ajmg.a.62496

18. Tatton-Brown, K. & Rahman, N. The NSD1 and EZH2 overgrowth genes, similarities and differences. *Am. J. Med. Genet. Part C Semin. Med. Genet.* **163**, 86–91 (2013).

19. Gibson, W. T. *et al.* Mutations in EZH2 cause weaver syndrome. *Am. J. Hum. Genet.* **90**, 110–118 (2012).

20. Tatton-Brown, K. *et al.* Germline mutations in the oncogene EZH2 cause Weaver syndrome and increased human height. *Oncotarget* **2**, 1127–1133 (2011).

21. Tatton-Brown, K. *et al.* Weaver syndrome and EZH2 mutations: Clarifying the clinical phenotype. *Am. J. Med. Genet. Part A* **161**, 2972–2980 (2013).

22. Hentze, M. W. & Kulozik, A. E. A perfect message: RNA surveillance and nonsense-mediated decay. *Cell* **96**, 307–310 (1999).

23. Imagawa, E. *et al.* Mutations in genes encoding polycomb repressive complex 2 subunits cause Weaver syndrome. *Hum. Mutat.* **38**, 637–648 (2017).

24. Cohen, A. S. A. A. *et al.* Weaver Syndrome-Associated EZH2 Protein Variants Show Impaired Histone

Methyltransferase Function In Vitro. *Hum. Mutat.* **37**, 301–307 (2016).

25. Lui, J. C. *et al.* Ezh2 Mutations Found in the Weaver Overgrowth Syndrome Cause a Partial Loss of H3K27 Histone Methyltransferase Activity. *J. Clin. Endocrinol. Metab.* **103**, 1470–1478 (2018).

26. Choufani, S. *et al.* DNA Methylation Signature for EZH2 Functionally Classifies Sequence Variants in Three PRC2 Complex Genes. *Am. J. Hum. Genet.* **106**, 596–610 (2020).

27. Brien, G. L. *et al.* Simultaneous disruption of PRC2 and enhancer function underlies histone H3.3-K27M oncogenic activity in human hindbrain neural stem cells. *Nat. Genet.* **53**, 1221–1232 (2021).

28. Conway, E. *et al.* BAP1 enhances Polycomb repression by counteracting widespread H2AK119ub1 deposition and chromatin condensation. *Mol. Cell* **81**, 3526-3541.e8 (2021).

29. Jain, S. U. *et al.* H3 K27M and EZHIP Impede H3K27-Methylation Spreading by Inhibiting Allosterically Stimulated PRC2. *Mol. Cell* **80**, 726-735.e7 (2020).

30. McCabe, M. T. *et al.* Mutation of A677 in histone methyltransferase EZH2 in human B-cell lymphoma promotes hypertrimethylation of histone H3 on lysine 27 (H3K27). *Proc. Natl. Acad. Sci. U. S. A.* **109**, 2989–2994 (2012).

31. Sneeringer, C. J. *et al.* Coordinated activities of wild-type plus mutant EZH2 drive tumor-associated hypertrimethylation of lysine 27 on histone H3 (H3K27) in human B-cell lymphomas. *Proc. Natl. Acad. Sci. U. S. A.* **107**, 20980–20985 (2010).

32. Højfeldt, J. W. *et al.* Accurate H3K27 methylation can be established de novo by SUZ12-directed PRC2. *Nat. Struct. Mol. Biol.* **25**, 225–232 (2018).

33. Ricci, M. A., Manzo, C., García-Parajo, M. F., Lakadamyali, M. & Cosma, M. P. Chromatin Fibers Are Formed by Heterogeneous Groups of Nucleosomes In Vivo. *Cell* **160**, 1145–1158 (2015).

34. Douglas, G. *et al.* De novo missense variants in MEIS2 recapitulate the microdeletion phenotype of cardiac and palate abnormalities, developmental delay, intellectual disability and dysmorphic features. *Am. J. Med. Genet. Part A* **176**, 1845–1851 (2018).

35. Tatton-Brown, K. *et al.* Mutations in Epigenetic Regulation Genes Are a Major Cause of Overgrowth with Intellectual Disability. *Am. J. Hum. Genet.* **100**, 725–736 (2017).

36. Heidet, L. *et al.* Targeted exome sequencing identifies PBX1 as involved in monogenic congenital anomalies of the kidney and urinary tract. *J. Am. Soc. Nephrol.* **28**, 2901–2914 (2017).

37. Slavotinek, A. *et al.* De novo, deleterious sequence variants that alter the transcriptional activity of the homeoprotein PBX1 are associated with intellectual disability and pleiotropic developmental defects. *Hum. Mol. Genet.* **26**, 4849–4860 (2017).

38. Choi, J. *et al.* Oculodentodigital Dysplasia with a Novel Mutation in GJA1 Diagnosed by Targeted Gene Panel Sequencing: A Case Report and Literature Review - PubMed. *Ann Clin Lab Sci* **48**, 776–781 (2018).

39. Alcantara, D. *et al.* Mutations of AKT3 are associated with a wide spectrum of developmental disorders including extreme megalencephaly. *Brain* **140**, 2610–2622 (2017).

40. Mitchell, K. J. *et al.* Functional analysis of secreted and transmembrane proteins critical to mouse development. **28**, (2001).

41. Ohkubo, N. *et al.* Abnormal Behaviors and Developmental Disorder of Hippocampus in Zinc Finger Protein 521 (ZFP521) Mutant Mice. *PLoS One* **9**, e92848 (2014).

42. Kamien, B. *et al.* A Clinical Review of Generalized Overgrowth Syndromes in the Era of Massively Parallel Sequencing. *Mol. Syndromol.* **9**, 70–82 (2018).

43. Ernst, J. & Kellis, M. Discovery and characterization of chromatin states for systematic annotation of the human genome. *Nat. Biotechnol.* **28**, 817–825 (2010).

44. GroB, A. *et al.* Tumorigenic and antiproliferative properties of the TALE-transcription factors MEIS2D and MEIS2A in neuroblastoma. *Cancer Res.* **78**, 1935–1947 (2018).

45. Kondo, T. *et al.* Polycomb Potentiates Meis2 Activation in Midbrain by Mediating Interaction of the Promoter with a Tissue-Specific Enhancer. *Dev. Cell* **28**, 94–101 (2014).

46. Chang, C. P. *et al.* Meis proteins are major in vivo DNA binding partners for wild-type but not chimeric Pbx proteins. *Mol. Cell. Biol.* **17**, 5679 (1997).

47. Rivière, J. B. *et al.* De novo germline and postzygotic mutations in AKT3, PIK3R2 and PIK3CA cause a spectrum of related megalencephaly syndromes. *Nat. Genet. 2012 448* **44**, 934–940 (2012).

48. Engelman, J. A., Luo, J. & Cantley, L. C. The evolution of phosphatidylinositol 3-kinases as regulators of growth and metabolism. *Nat. Rev. Genet. 2006 78* **7**, 606–619 (2006).

49. Poduri, A. *et al.* Somatic activation of AKT3 causes hemispheric developmental brain malformations. *Neuron* **74**, 41–48 (2012).

50. Pizzuti, A. *et al.* A homozygous GJA1 gene mutation causes a Hallermann-Streiff/ODDD spectrum phenotype. *Hum. Mutat.* **23**, 286 (2004).

51. Easton, R. M. *et al.* Role for Akt3/Protein Kinase B in Attainment of Normal Brain Size. *Mol. Cell. Biol.* **25**, 1869–1878 (2005).

52. Blake, J. A. *et al.* Mouse Genome Database (MGD): Knowledgebase for mouse–human comparative biology. *Nucleic Acids Res.* **49**, D981–D987 (2021).

53. Wu, M. *et al.* Zfp521 antagonizes Runx2, delays osteoblast differentiation in vitro, and promotes bone formation in vivo. *Bone* **44**, 528–536 (2009).

54. Xu, R. *et al.* OLIG2 Drives Abnormal Neurodevelopmental Phenotypes in Human iPSC-Based Organoid and Chimeric Mouse Models of Down Syndrome. *Cell Stem Cell* **24**, 908-926.e8 (2019).

55. Chakrabarti, L. *et al.* Olig1 and Olig2 triplication causes developmental brain defects in Down syndrome. *Nat. Neurosci. 2010 138* **13**, 927–934 (2010).

56. Szu, J., Wojcinski, A., Jiang, P. & Kesari, S. Impact of the Olig Family on Neurodevelopmental Disorders. *Front. Neurosci.* **15**, 332 (2021).

57. Gamu, D. & Gibson, W. T. Reciprocal skeletal phenotypes of PRC2-related overgrowth and Rubinstein–Taybi syndromes: potential role of H3K27 modifications. *Cold Spring Harbor Molecular Case Studies* **6**, (2020).

58. Cuddapah, V. A. *et al.* Understanding the phenotypic spectrum of ASXL-related disease: Ten cases and a review of the literature. (2021). doi:10.1002/ajmg.a.62156

59. Alfert, A., Moreno, N. & Kerl, K. The BAF complex in development and disease. *Epigenetics Chromatin 2019 121* **12**, 1–15 (2019).

60. Conway, E. *et al.* A Family of Vertebrate-Specific Polycombs Encoded by the LCOR / LCORL Genes Balance PRC2 Subtype Activities. *Mol. Cell* **70**, 408-421.e8 (2018).

61. Tokunaga, M., Imamoto, N. & Sakata-Sogawa, K. Highly inclined thin illumination enables clear single-molecule imaging in cells. *Nat. Methods* **5**, 159–161 (2007).

62. Ovesný, M., Křížek, P., Borkovec, J., Švindrych, Z. & Hagen, G. M. ThunderSTORM: a comprehensive ImageJ plug-in for PALM and STORM data analysis and super-resolution imaging. *Bioinformatics* **30**, 2389–2390 (2014).

63. Williamson, D. J. *et al.* Machine learning for cluster analysis of localization microscopy data. *Nat. Commun. 2020 111* **11**, 1–10 (2020).

64. Langmead, B. & Salzberg, S. L. Fast gapped-read alignment with Bowtie 2. *Nat. Methods* **9**, 357–359 (2012).

65. Orlando, D. A. *et al.* Quantitative ChIP-Seq normalization reveals global modulation of the epigenome. *Cell Rep.* **9**, 1163–1170 (2014).

66. Li, H. *et al.* The Sequence Alignment/Map format and SAMtools. *Bioinformatics* **25**, 2078–2079 (2009).

67. Ramírez, F. *et al.* deepTools2: a next generation web server for deep-sequencing data analysis. *Nucleic Acids Res.* **44**, W160–W165 (2016).

68. Quinlan, A. R. & Hall, I. M. BEDTools: A flexible suite of utilities for comparing genomic features. *Bioinformatics* **26**, 841–842 (2010).

69. Heinz, S. *et al.* Simple Combinations of Lineage-Determining Transcription Factors Prime cis-Regulatory Elements Required for Macrophage and B Cell Identities. *Mol. Cell* **38**, 576–589 (2010).

70. Amemiya, H. M., Kundaje, A. & Boyle, A. P. The ENCODE Blacklist: Identification of Problematic Regions of the Genome. *Sci. Rep.* **9**, (2019).

71. Martin, M. Cutadapt removes adapter sequences from high-throughput sequencing reads. *EMBnet.journal* **17**, 10–12 (2011).

72. Dobin, A. *et al.* STAR: ultrafast universal RNA-seq aligner. *Bioinformatics* **29**, 15–21 (2013).

73. Liao, Y., Smyth, G. K. & Shi, W. FeatureCounts: An efficient general purpose program for assigning sequence reads to genomic features. *Bioinformatics* **30**, 923–930 (2014).

74. Love, M. I., Huber, W. & Anders, S. Moderated estimation of fold change and dispersion for RNA-seq data with DESeq2. *Genome Biol.* **15**, 1–21 (2014).

75. Usemann, J., Ernst, T., Schäfer, V., Lehmberg, K. & Seeger, K. EZH2 mutation in an adolescent with Weaver syndrome developing acute myeloid leukemia and secondary hemophagocytic lymphohistiocytosis. *Am. J. Med. Genet. Part A* **170**, 1274–1277 (2016).

76. Choufani, S. *et al.* DNA Methylation Signature for EZH2 Functionally Classifies Sequence Variants in Three PRC2 Complex Genes. *Am. J. Hum. Genet.* **106**, 596–610 (2020).

77. Paraskevopoulou, N. & Gevers, E. Case report: Tall stature, obesity and hip dysplasia in Weaver syndrome due to a loss-of-function variant in EHZ2. in *European Society for Paediatric Endocrinology* **94**, (2021).

78. Oh, I. *et al.* First Korean Case of Weaver Syndrome Along with Neuroblastoma and Genetic Confirmation of EZH2 Variant. *Lab. Med. Online* **13**, 48–52 (2023).

79. Al-Salem, A., Alshammari, M. J., Hassan, H., Alazami, A. M. & Alkuraya, F. S. Weaver syndrome and defective cortical development: A rare association. *Am. J. Med. Genet. Part A* **161**, 225–227 (2013).

80. Kasinath, V. *et al.* JARID2 and AEBP2 regulate PRC2 in the presence of H2AK119ub1 and other histone modifications. *Science (80-.).* **371**, (2021).

81. Su, I.-H. *et al.* Ezh2 controls B cell development through histone H3 methylation and Igh rearrangement. (2002). doi:10.1038/ni876

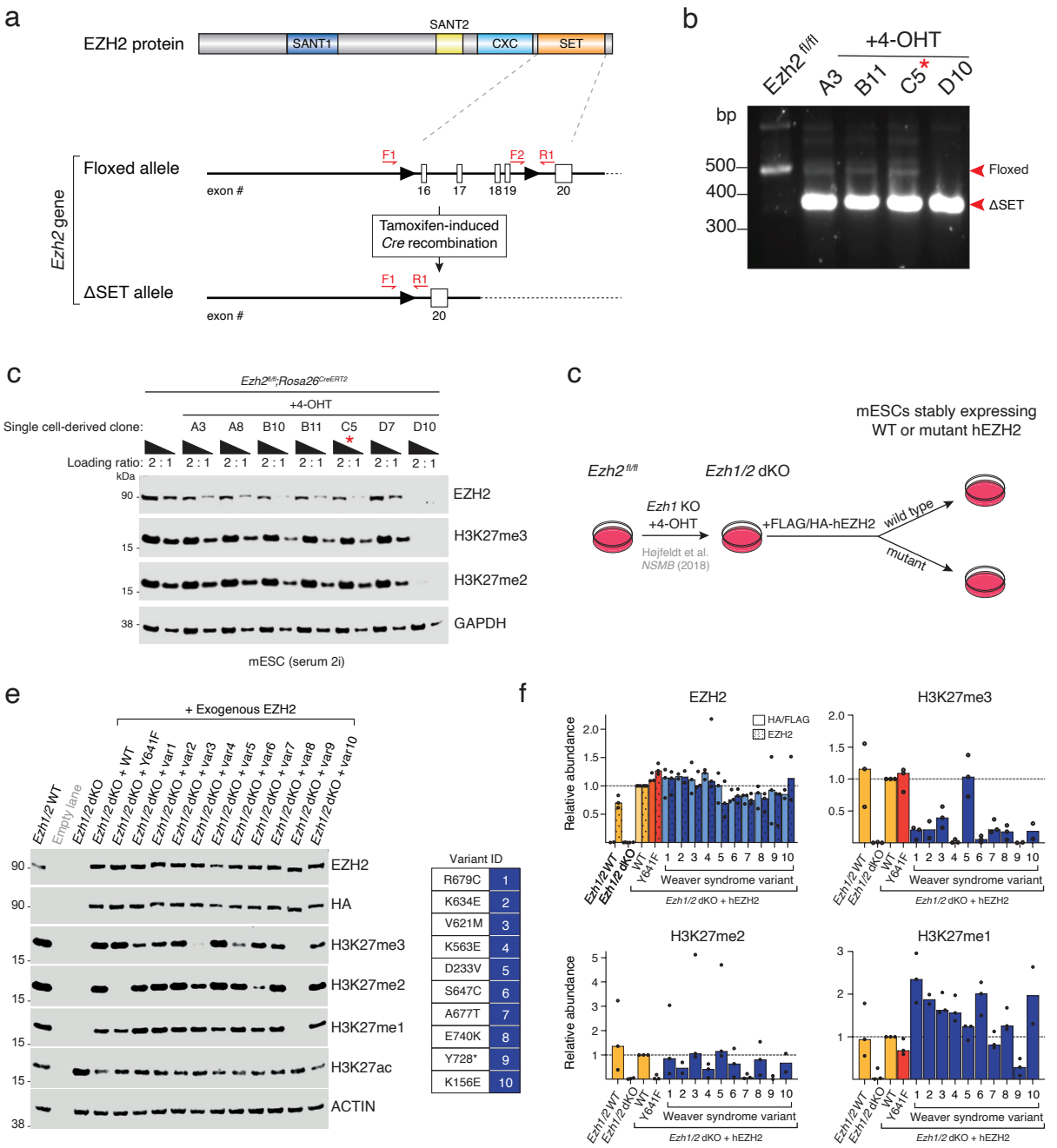

Extended Data Figure 1. Weaver syndrome-associated EZH2 variants dominant negatively impair PRC2 activity. a. (Top) Schematic of the mouse EZH2 protein showing key domains. (Bottom) Schematic representation of the *Ezh2*-targeted locus before and after Cre-mediated recombination. SET domain-encoding exons are numbered and displayed as open boxes, while *loxP* sequences are depicted by arrows. Genotyping PCR primers are indicated in red. This gene targeting strategy was originally devised by the Tarakhovsky lab[81]. **b.** A representative genotyping PCR agarose gel using the primers indicated in (a), confirming heterozygous (A3, B11, C5) or homozygous (D10) knockout of the *Ezh2* SET domain-encoding exons. The asterisk indicates the clone (C5) that was taken forward as the parental Ezh2$^{fl/\Delta}$ cell line for all subsequent experiments. **c.** Immunoblots for EZH2, H3K27me3 and H3K27me2, probing whole cell lysates from the indicated cell lines. GAPDH is shown as a loading control. The asterisk indicates the clone (C5) that was taken forward as the parental Ezh2$^{fl/\Delta}$ cell line for all subsequent experiments. **d.** Schematic of the isogenic stem cell model system used to generate the data presented in panels e and f, involving expression of exogenous EZH2 constructs in *Ezh1/2* double knockout (dKO) mouse embryonic stem cells. **e.** Representative immunoblots for HA, EZH2, and H3K27 modification states, probing whole cell lysates from the indicated cell lines. β-ACTIN is shown as a loading control. **f.** Relative quantification of immunoblot analyses of EZH2 and the HA/FLAG epitope tag, H3K27me3, H3K27me2 and H3K27me1 abundance in the indicated cell lines. Signal intensity values were normalized to a loading control and then expressed relative to the *Ezh1/2* dKO + EZH2-WT cell line. The dashed line represents the normalised *Ezh1/2* dKO + EZH2-WT value. Data values represent independent biological replicates whose median values are plotted as bars.

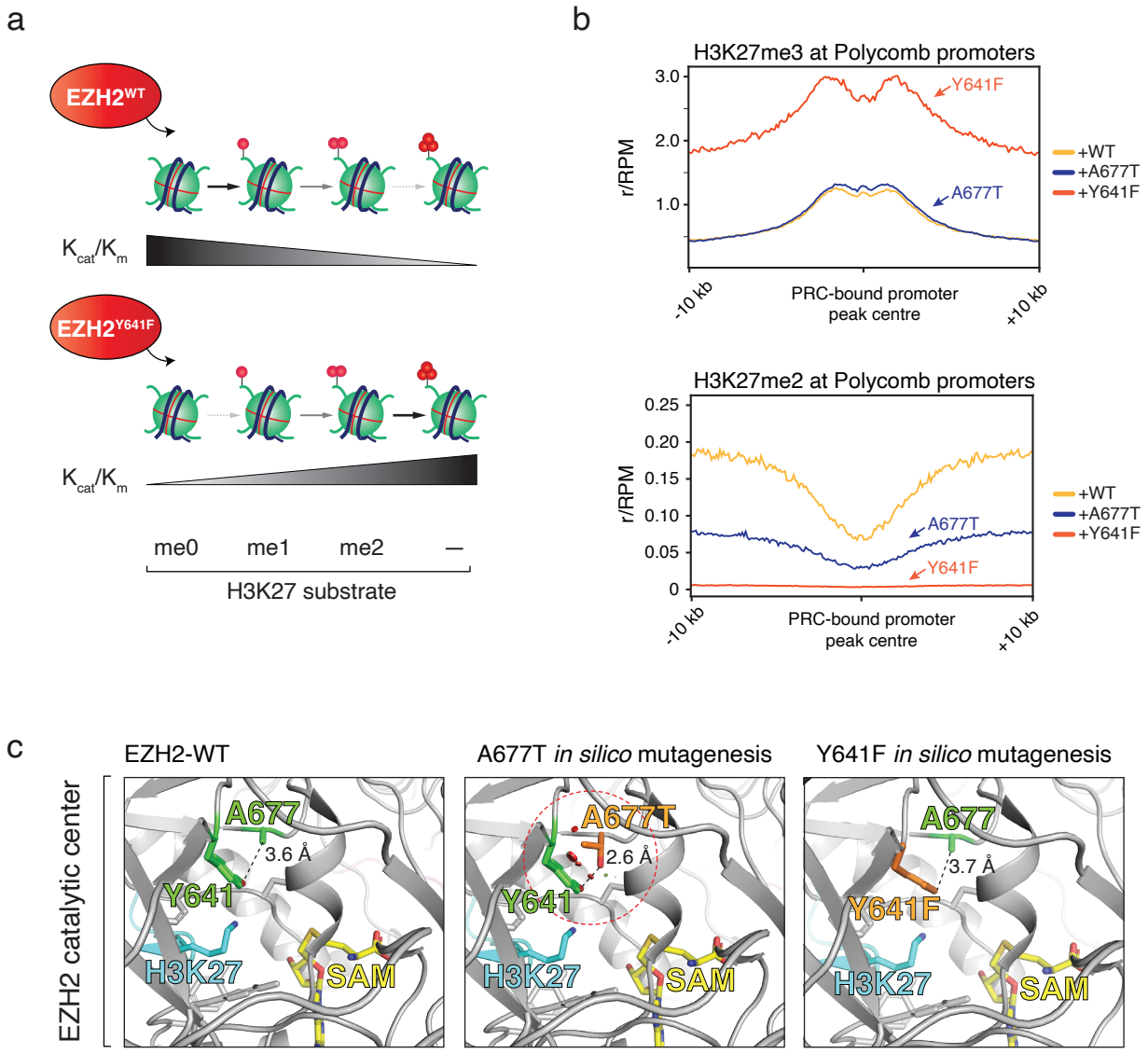

Extended Data Figure 2. Weaver syndrome-associated EZH2 mutations differ in their effects on H3K27me3 at Polycomb target genes. a. Schematic illustrating PRC2-mediated H3K27me3 deposition at Polycomb target genes, where Kcat/Km indicates the catalytic efficiency of PRC2. **b.** Average ChIP-Rx signal profiles for H3K27me3 (top) and H3K27me2 (bottom) at PRC2-bound promoters (n = 3870) in Ezh2$^{fl/\Delta}$ ESCs expressing either EZH2-WT (yellow), EZH2-A677T (blue) or EZH2-Y641F (red). Data represents a biologically independent experiment (r2) from that presented in Figure 3C. **c.** Images of the in-silico mutagenesis of EZH2 to model the Weaver syndrome-associated hEZH2-A677T variant (middle) and the oncogenic hEZH2-Y641F (right), in the context of PRC2.2 with a substrate nucleosome (PDB 6WKR). The wild-type A677 and Y641 amino acids are coloured in green, with their corresponding mutated amino acids superimposed and coloured in orange. The substrate histone tail is in cyan, SAM is in yellow, and all other EZH2 residues are in grey. In the image of the A667T in-silico mutagenesis, steric (van der Waals) clashes between T677 and Y641 are represented by red discs (circled in red), while the dashed line indicates a short distance between the hydroxyls of both residues (2.6 Å).

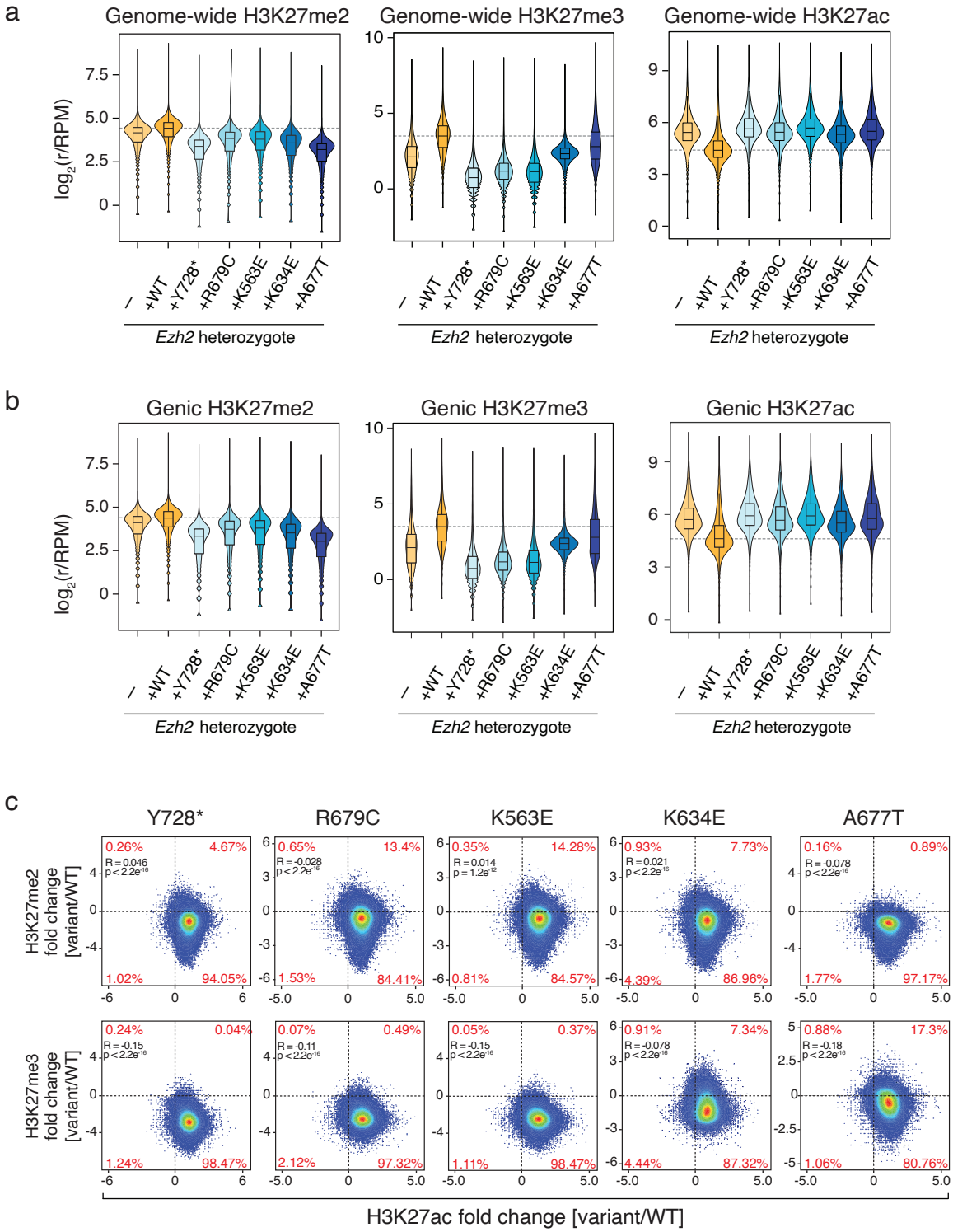

Extended Data Figure 3. Weaver syndrome-associated EZH2 variants alter the intergenic landscape of H3K27 modifications and chromatin compaction. a. Violin plot representations of the total (genome wide) log2 ChIP-Rx normalized reads per million (r/RPM) of H3K27me2, H3K27me3 and H3K27ac enrichments in the indicated cell lines across 272,477 10kb bins. Control cell lines are coloured yellow while Weaver syndrome cell models are coloured blue. The dashed lines represent the Ezh2$^{fl/\Delta}$ + EZH2-WT values. **b.** Violin plot representations of the log2 ChIP-Rx normalized reads per million (r/RPM) of H3K27me2, H3K27me3 and H3K27ac enrichments in the indicated cell lines across 196,505 10kb bins representing all gene bodies. Control cell lines are coloured yellow while Weaver syndrome cell models are coloured blue. The dashed lines represent the Ezh2$^{fl/\Delta}$ + EZH2-WT values. **c.** Correlation plots demonstrating the relationship between changes in genome-wide ChIP-Rx enrichment of H3K27me2 (top row) or H3K27me3 (bottom row) and H3K27ac in cells expressing the indicated Weaver syndrome EZH2 variants compared to EZH2-WT. The percentage of 10kb bins in each quadrant is indicated. The p value and correlation coefficient were calculated using Pearson's correlation.

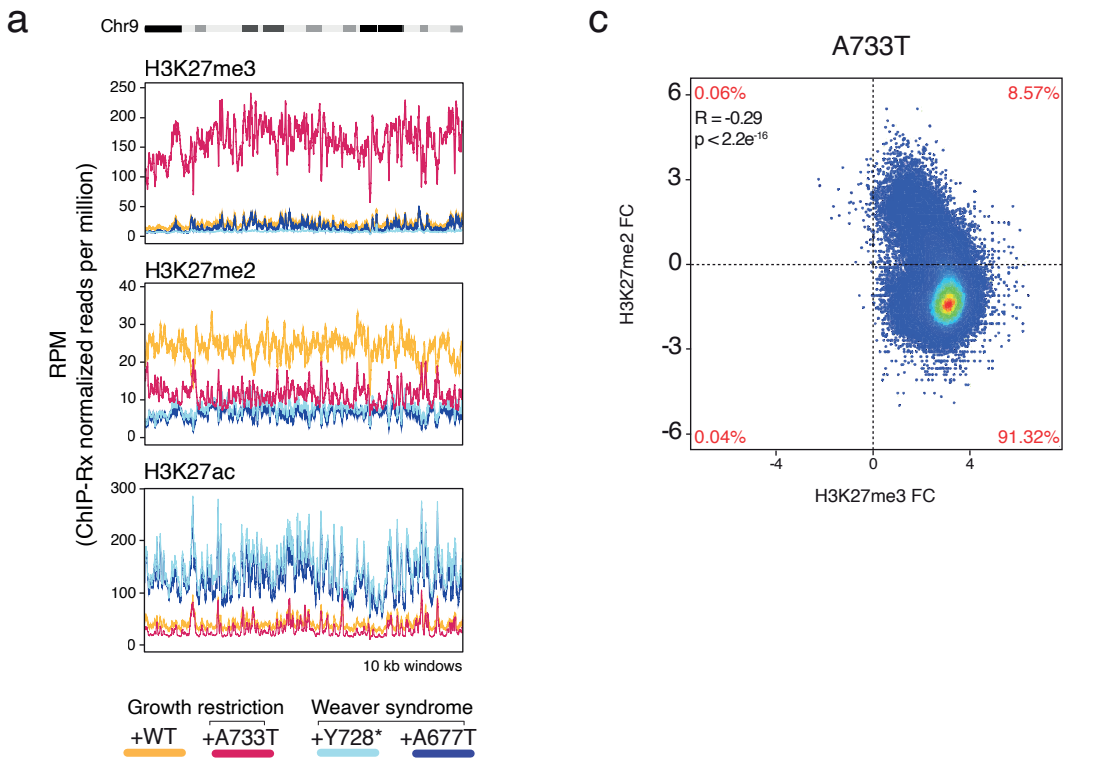

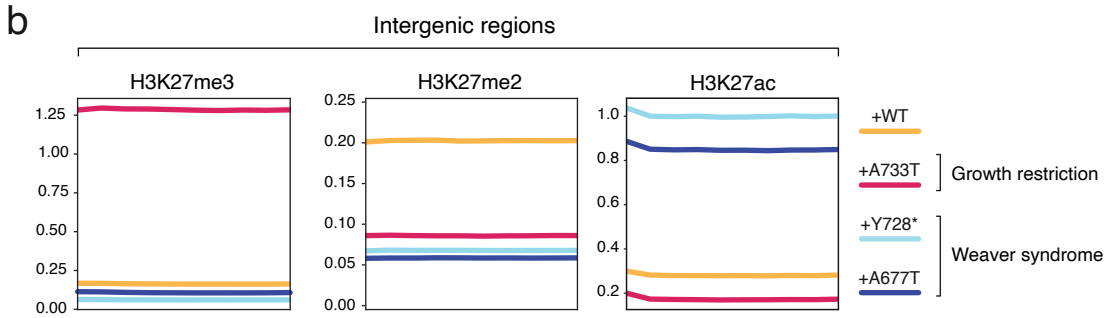

Extended Data Figure 4. An EZH2 mutation associated with growth restriction induces opposing histone modification changes. a. Rolling average plots presenting the fold change in H3K27me3, H3K27me2 and H3K27ac ChIP-Rx signal in Ezh2$^{fl/\Delta}$ cells expressing growth restriction (pink) or Weaver syndrome (blue) EZH2 variants or wild-type EZH2 (yellow) across the whole of chromosome 9. **b.** Average ChIP-Rx signal profiles for H3K27me3, H3K27me2 and H3K27ac at intergenic regions in Ezh2$^{fl/\Delta}$ cells expressing growth restriction (pink) or Weaver syndrome (blue) EZH2 variants or wild-type EZH2 (yellow). **c.** Correlation plot demonstrating the relationship between changes in genome-wide ChIP-Rx enrichment of H3K27me2 and H3K27me3 in the growth restriction-associated EZH2 variant cell line, compared to wild-type EZH2. The percentage of 10kb bins in each quadrant is indicated. The p value and correlation coefficient were calculated using Pearson's correlation.

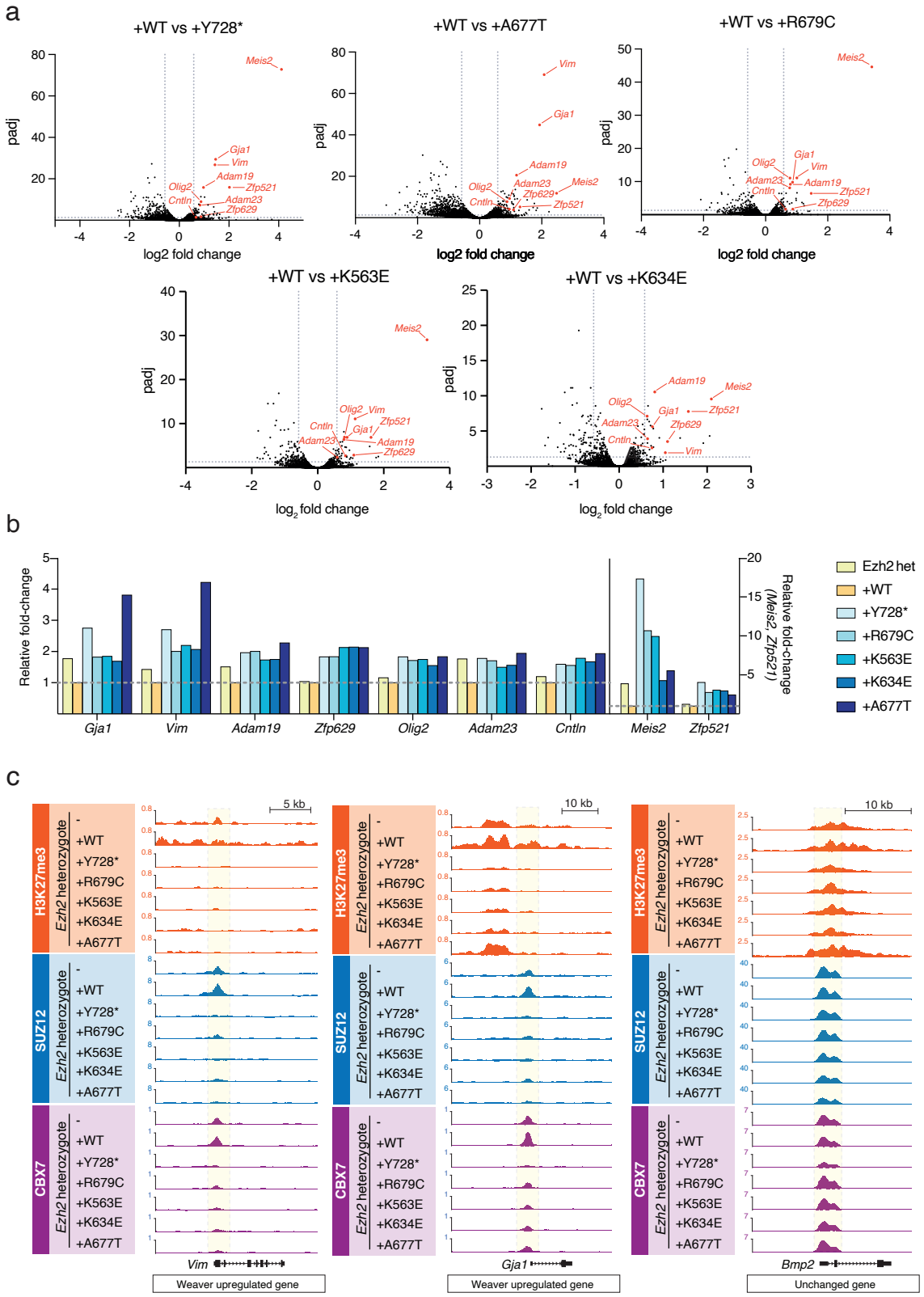

Extended Data Figure 5. The growth restriction-associated EZH2 variant causes opposite chromatin and transcriptional changes at Polycomb target genes compared to Weaver Syndrome EZH2 variants. **a.** Volcano plots representing genes with differentially abundant RNA transcripts in RNAseq of cells expressing the indicated WS-associated EZH2 variants versus wild-type EZH2. The cohort of commonly upregulated genes are highlighted in red. **b.** Bar chart representing mean expression levels of the cohort of upregulated genes across three biologically independent RNAseq replicate experiments in the indicated cell lines. **c.** UCSC genome browser tracks showing ChIP-Rx normalised reads of H3K27me3, SUZ12 and CBX7 in the indicated cell lines at a gene upregulated in WS variant cell lines (*Akt3*) and two Polycomb target genes which did not change in expression levels (*Cnr1, Atf3*).

Tables

Table 1. Weaver syndrome-associated single amino acid variants of EZH2

hEZH2 residue		Variant ID (this study)	Protein Domain	# Affected individuals	Source citation(s)
Wild type	Weaver syndrome				
R25	Q			3	Tatton-Brown et al., 2013
D124	V		Just upstream of SRM	1	Choufani et al., 2020
N130	K			1	Tatton-Brown et al., 2013
P132	L			1	Usemann et al., 2016
	S			2	Cohen et al., 2016; Gibson et al., 2012
Y133	C			2	Cohen et al., 2016
M134	T			1	Tatton-Brown et al., 2011
F145	L		SRM	1	Tatton-Brown et al., 2013
E148	G			1	Tatton-Brown et al., 2013
	K			1	Tatton-Brown et al., 2013
Y153	C			1	Tatton-Brown et al., 2013
	del			1	Cohen et al., 2016
K156	E	10		6	Tatton-Brown et al., 2011
G159	R			1	Tatton-Brown et al., 2013
D233	V	5	SANT1	2	Tatton-Brown et al., 2013
H279	R		MCSS	1	Tatton-Brown et al., 2011
	Y			2	Tatton-Brown et al., 2017
K563	E	4	CXC	1	Tatton-Brown et al., 2013
H613	Y		SET	1	Tatton-Brown et al., 2013
V621	M	3		3	Lui et al., 2018; Paraskevopoulou & Gevers, 2021; Tatton-Brown et al., 2011
K634	E	2		1	Tatton-Brown et al., 2011
S647	C	6		2	Tatton-Brown et al., 2013
D649	G			2	Tatton-Brown et al., 2013
A651	T			2	Choufani et al., 2020
Y658	N			1	Tatton-Brown et al., 2011
D659	V			1	Tatton-Brown et al., 2011
S664	N			1	Choufani et al., 2020
N668	Y			1	Tatton-Brown et al., 2013
A677	T	7		1	Tatton-Brown et al., 2011
R679	C	1		7	Tatton-Brown et al., 2011; Tatton-Brown et al., 2013; Oh et al. 2023
	H			1	Tatton-Brown et al., 2013
H689	Y			1	Gibson et al., 2012
S690	L			1	Tatton-Brown et al., 2011
H706	R			1	Tatton-Brown et al., 2013
Y728	*	9		1	Tatton-Brown et al., 2011
S729	G			1	Tatton-Brown et al., 2013
Q730	H			1	Tatton-Brown et al., 2013
Y736	C			1	Tatton-Brown et al., 2011
E740	K	8		2	Al-Salem et al., 2013; Tatton-Brown et al., 2011
	V			1	Choufani et al., 2020

Table 2. Antibodies used in this study

Target	Source	Western blot	ChIP
EZH2	BD43 (Bracken lab)	1:10	-
EZH2	Abcam (ab191250)	1:1000	-
SUZ12	Cell Signalling (3737)	1:2000	1µg
EED	Cell Signalling (51673S)	1:500	-
H3K27ac	Abcam (ab4729)	1:1000	2µg
H3K27ac	Sigma-Aldrich (07-360)	1:1000	-
H3K27me1	Active Motif (0321)	1:2000	-
H3K27me2	Cell Signalling (9728S)	1:2000	2.25µg
H3K27me3	Cell Signalling (custom)	-	1µg
H3K27me3	Active Motif (0323)	1:2500	-
HA	Cell Signalling (3724)	1:1000	-
FLAG	Sigma-Aldrich (clone M2)	1:1000	
ACTIN	Proteintech (60008-1-Ig)	1:5000	-
GAPDH	Proteintech (60004-1-Ig)	1:5000	-
VINCULIN	Cell Signalling (4650)	1:2500	-
CBX7	Abcam (ab21873)	-	2µg
Mouse IgG	Millipore (12-371)	-	2µg